Lawrence Livermore National Laboratory

Electrochemical behavior of $SnCl_2$ and influence of Cu and Ni ions in molten LiCl–KCl–$CaCl_2$ eutectic

D Roberts

January 2026

Journal of the Electrochemical Society

Disclaimer

This work performed under the auspices of the U.S. Department of Energy by Lawrence Livermore National Laboratory under Contract DE-AC52-07NA27344.

Electrochemical behavior of $SnCl_2$ and influence of Cu and Ni ions in molten LiCl−KCl−$CaCl_2$ eutectic

Bryant Johnson[a,*], Ricardo Rodriguez-Ceron[a], Carlos Mejia[a], Tatiana Ayers[b], Gabrielle Dangel[b], Molly Garner[b], Devin Rappleye[a]

[a] Department of Chemical and Biological Engineering, Brigham Young University, Provo, UT 84602 USA
[b] Savannah River National Laboratory, Aiken, SC 29808 USA

Abstract

This study investigates the electrochemical behavior and properties of $SnCl_2$ in a eutectic LiCl−KCl−$CaCl_2$ molten salt system. The Sn^{2+}/Sn redox couple was confirmed to be a reversible two-electron exchange reaction by square wave voltammetry (SWV). The diffusivity of the Sn^{2+} ion was determined using chronoamperometry (CA), chronopotentiometry (CP), and cyclic voltammetry (CV) at 685 K. Most importantly, standard reduction potentials were calculated from open-circuit potential (OCP) data. Furthermore, the influence of Cu and Ni ions on the system was explored. This foundational research provides critical data for future studies in the management of impurities in select metal refining processes.

1.0 Introduction

Molten salts are widely used in high-temperature purification, metal extraction, and alloy formation across many industries. They are particularly suited for the separation of molten metals. Applications involving tin (Sn) in molten salts have become increasingly common, underscoring the need for chemical and electrochemical understanding of Sn behavior in molten salts. From the profitable recovery of Sn metal from indium-tin oxide (ITO) waste [1, 2], to the production of Sn-based alloys for lithium-ion batteries [3, 4] and zirconium-tin alloys as nuclear fuel cladding with improved corrosion resistance and mechanical properties [5, 6], the electrochemistry of Sn in molten salts plays a critical role in emerging technologies. Sn has also been identified as a possible surrogate for plutonium electrorefining [7, 8]. Thus, understanding Sn electrochemistry in molten salts is essential for advancing these applications.

Previous studies have examined Sn electrochemistry in various molten salts. In the eutectic LiCl−KCl, the standard potential of the Sn^{2+}/Sn couple has been calculated [9–11], along with the rate constant and the charge transfer coefficient at tungsten and liquid-tin electrodes [12, 13]. Standard potentials have been reported in disagreement with each other for the Sn^{4+}/Sn^{2+} couple [10, 11, 14] due to the volatile condition of $SnCl_4$ [12]. The diffusivity of the Sn^{2+}/Sn couple in LiCl−KCl has been reported at several temperatures [2, 3, 11]. Beyond the LiCl−KCl eutectic, the standard potential for the Sn^{2+}/Sn couple has been reported in NaCl−KCl [15], $MgCl_2$−NaCl−KCl, and $MgCl_2$−KCl [16]. Several electrochemical studies have been conducted in

different mixtures of $AlCl_3$ at temperatures below the melting point of Sn metal [17–20]. Dilute $SnCl_2$ mixtures in $ZnCl_2$−NaCl have also been studied to determine the effect of $ZnCl_2$ concentration on the electrochemical behavior of Sn ions [21]. Despite these efforts, the electrochemistry of Sn in LiCl–KCl–$CaCl_2$ eutectic remains unstudied, even though this system offers advantages for oxide reduction and electrorefining.

Given these gaps and the advantages of LiCl−KCl−$CaCl_2$, studying this system can elucidate electrochemical properties and behavior to support the development and optimization of Sn electrochemical processing. Both eutectic compositions of LiCl−KCl−$CaCl_2$ have been characterized as low-temperature electrolytes for oxide reduction [22, 23], as occurs in ITO recovery [1]. The $CaCl_2$-deficient ternary system (50.5−44.2−5.3 mol%) allows a lower operating temperature due to its lower melting point at 605 K, reducing corrosion and expanding material options. Furthermore, the relatively low boiling temperature of $SnCl_2$ (896 K) necessitates a lower-temperature molten salt for electrorefining where $SnCl_2$ acts as a charge carrier [7]. Because of these advantages, the electrochemical behavior of Sn in LiCl−KCl−$CaCl_2$ eutectic (50.5−44.2−5.3 mol%) is investigated herein.

Realizing these advantages requires reliable data on fundamental electrochemical properties. Accurate standard potential data enables precise control over the selectivity and product purity in electrochemical separations, while diffusivity data allows prediction of separation rates. By quantifying the standard potential and diffusivity of $SnCl_2$ in LiCl−KCl−$CaCl_2$, improvements to separation selectivity and rate can be achieved with greater insight.

To the authors' knowledge, this is the first electrochemical study of $SnCl_2$ in LiCl−KCl−$CaCl_2$ molten salt. Understanding Sn's electrochemistry supports advancing its electrochemical separation in this system. Nickel (Ni) and copper (Cu) impurities are of particular interest because their standard potentials are close to that of Sn^{2+}/Sn, and they commonly occur with Sn in structural materials, electronics, and feed ore [24, 25]. Their presence can influence separation feasibility. This work investigates the electrochemical behavior and quantifies standard potential and diffusivity of $SnCl_2$ in LiCl−KCl−$CaCl_2$ and examines the influence of Cu and Ni ions on the electrochemical behavior and properties of Sn. These properties will inform physics-based models and process optimization, paving the way for more efficient and selective separations.

2.0 Experimental Methods

2.1 Materials and Apparatus

All electrochemical experiments were carried out inside an inert-atmosphere, argon-filled glovebox (<2 ppm O_2/H_2O). Molten salt samples were held in alumina crucibles (Advalue Technology, AL-2100) and heated inside of a tube furnace (MTI, OTF-1200X-S-NT). In each run,

an alumina tube was used to position the alumina crucibles in the heating zone of the furnace. A nickel tube was placed around the crucibles to serve as a Faraday cage for the electrochemical experiments. Electrochemical measurements were acquired using an Autolab potentiostat (PGSTAT302N) controlled by NOVA 2.1.7 software.

The $SnCl_2$ (anhydrous, 99% min, Thermo Scientific Chemicals, 041960.30), LiCl (ACS, 99% min, Thermo Scientific Chemicals, 036217.A3), KCl (ACS, >99.0%, Thermo Scientific Chemicals 011595.A7), and $CaCl_2$ (dihydrate, ACS, >99.0%, Thermo Scientific Chemicals, 33296) were dried in an oven (Across International, AT32x-316L) under vacuum. $SnCl_2$ was dried for 24 hours at 348 K and 8 hours at 428 K. LiCl and KCl were dried at 503 K for 48 hours. $CaCl_2$ was dried using the following procedure: 5 hours at 303 K, 11 hours at 363 K, 8 hours at 393 K, 48 hours at 503 K. After each salt was dried and transferred into the glovebox, a salt block of eutectic LiCl−KCl−$CaCl_2$ (50.5−44.2−5.3 mol%) was made by placing the appropriate amounts of each component salt into a large alumina crucible (Advalue Technology, AL-21000) and heating it in a furnace to 1023 K. The furnace was held at 1023 K for 3 hours to allow the eutectic to form. After 3 hours, the furnace was cooled, and the salt block was removed from the large alumina crucible. Clean white pieces of the salt block were used for all electrochemical experiments and for the reference electrode (RE). The $NiCl_2$ (Thermo Fisher Scientific, ultra dry, 99.9%, metals basis, 0.35713.06) was added to the appropriate crucible with the eutectic salt at room temperature before an experimental run. A copper rod (McMster-Carr, 1/8” multipurpose 110 copper, 99.9%, 8966K71) was used to introduce Cu^+ to the salt bath by anodic dissolution at 0.2 V vs. RE for 26 s at 683 K.

A 5.0 mol% silver-silver chloride (Ag/AgCl) RE for all runs was prepared by placing 4.848 g of eutectic salt and 0.607 g of AgCl (99.997% metals basis, Alfa Aesar, 10857) into a thin-walled (0.46 mm), one-end-closed borosilicate NMR tube (10 mm OD, 9 in length, 100 MHz, Class A glass, 12012023). The salts were melted by slowly heating the tube and salts in a furnace to 683 K. A 0.25 mm Ag wire (99.9% metals basis, Thermo Scientific Chemicals, 012187.G9) was used as the contact in the reference solution and the electrical lead for the reference electrode. The Ag wire was sheathed above the salt with an alumina two bore tube pushed through a rubber stopper. After positioning the Ag wire and alumina sheath into the reference solution, the furnace was cooled slowly to avoid breaking the borosilicate tube. This reference electrode was used for all electrochemical measurements.

For all experiments, a 1.5-mm diameter tungsten (W) rod (99.95% metals basis, Thermo Scientific Chemicals, 042233.BV) served as the working electrode (WE), with a 3.175-mm W rod (99.95% metals basis, annealed, Thermo Scientific Chemicals, 010407.BY) as the counter electrode (CE). The WE and CE were sheathed above the molten salt by alumina tubes (AdValue Technology, AL-T-N1/4-N3/16-12). The RE, WE, and CE were raised and lowered using a vertical translator (Velmex, A2509P10-S2.5-TL, 0.0254 mm precision). The electrodes were aligned using a custom stainless steel lid and a custom aluminum attachment to the vertical translator. Temperature measurements were taken at the beginning and end of experiments by replacing

the CE with a type K thermocouple (DwyerOmega, Inconel 600, KMQIN-062U-12). A representation of the electrochemical cell is shown in Figure 1.

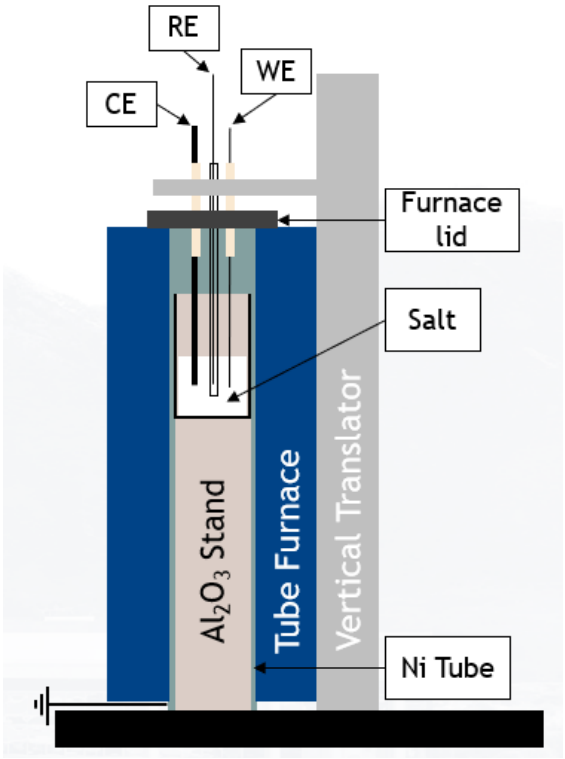

Figure 1: Depiction of Electrochemical cell set-up.

2.2 Electrochemical Techniques

2.2.1 Full Electrochemical Window

In each run, the upper and lower limit of the electrochemical window was established by cyclic voltammetry (CV). Electrochemical impedance spectroscopy (EIS) at the open-circuit potential E_{OCP} was used to measure the uncompensated solution resistance (R_s) [26]. The R_s value was taken to be the x-intercept of a Nyquist plot at a frequency around 10-100 kHz. Following EIS, a positive feedback test was conducted on a potential step with IR compensation to verify that the potentiostat was able to maintain stable potential setpoint changes within the required time intervals for CV and square-wave voltammetry (SWV) scan rates. Finally, ohmic drop (IR) compensation was applied during a full electrochemical window starting at 100% compensation and decreasing in value until instabilities in the electronic feedback loop (i.e. ringing) were eliminated. Once the optimal compensation percentage was determined, it was used during all applicable electrochemical measurements.

2.2.2 WE Surface Area

The WE surface area was determined by taking CV measurements at known height differences using the vertical translator to raise the WE a known, precise (0.0254 mm resolution) amount

[27]. A line was fit to the data points and the relationship between the change in WE surface area and peak height was established. The initial immersed area was calculated by finding the x-intercept as it represents the case of complete removal of the WE. The error was approximated by calculating the 95% confidence interval of the x-intercept. This relationship assumes that the effects of wicking are the same at each position and solution displacement is negligible. The WE surface area for each run was determined using this same method.

2.2.3 Square wave voltammetry (SWV)

SWV was used to quantify electron transfer and confirm reaction identification. To determine the number of electrons exchanged for a soluble-insoluble reaction with SWV data, the relation shown in Eq. 1 was used, where W_2 is the width of the back half at half-maximum of the reduction peak, R is the gas constant, T is the temperature at which the measurement was taken, F is Faraday's constant, and n is the number of electrons exchanged [28, 29]:

$$W_2 = 0.91\frac{RT}{nF}. \quad (1)$$

Eq. 1 assumes the following five conditions as detailed by Rappleye and Fuller [30]: (1) deposition onto an inert, foreign substrate, (2) resistance is well compensated, (3) W_2 is independent of frequency, (4) the absolute value of the pulse amplitude is between $0.8 \cdot RT/nF$ and $4.7 \cdot RT/nF$, and (5) the magnitude of the potential step is between $0.04 \cdot RT/nF$ and $0.23 \cdot RT/nF$. The relation shown in Eq. 2 was used for the analysis of soluble-soluble reaction data, where $W_{1/2}$ is the peak width at half height and $\xi = nF\Delta E/(RT) < 5$, with ΔE as the pulse amplitude [31, 32]:

$$W_{1/2} = \frac{RT}{nF}\left[3.53 + \frac{3.46\xi^2}{\xi+8.1}\right]. \quad (2)$$

2.2.4 Cyclic voltammetry (CV)

CV was used to identify the electrochemical reversibility of reactions and calculate the diffusivity of the analyte species. CV measurements were conducted using scan rates between 0.05 V/s and 1 V/s and a digital staircase step of 1 mV in the negative direction initially and the positive direction upon reversal. CVs were collected by applying scan rates in a random order to avoid introducing a bias. Four scans were performed at each scan rate to verify repeatability, with the third scan being used for all analysis.

For the electrodeposition of metal, the common relationship for reversible reactions is the Berzins-Delahay equation [33]:

$$I_p = 0.6105AC_o^*\sqrt{D_o\frac{n^3F^3}{RT}v}, \quad (3)$$

where I_p is the peak current, A is the surface area of the electrode, C_o^* is the bulk concentration of the oxidized species, D_o is the diffusivity of the oxidized species, and v is the scan rate. By regressing peak height versus the square root of scan rate, the slope of the line can be related to Eq. 3 to calculate diffusivity. The error can be found by propagating the regressed slope error with the error of the area, concentration, and temperature.

The semi-integration method was also used to quantify diffusivities based on CV data. Semi-integration analysis of CV is particularly useful, because the species solubility is irrelevant [34]. When the reaction is diffusion controlled, the semi-integral of the CV data plateaus and can be described by Eq. 4:

$$m^* = -nFAC_o^*\sqrt{D_o}\,, \tag{4}$$

where m^* is the semi-integral limiting current. The semi-integration technique uniquely allows the analysis of mixed systems by subtracting the plateaued m^* value of an initial reduced species from the plateaued m^* value of a co-deposition reaction. The diffusivity from each CV can be calculated separately using Eq. 4 and an average diffusivity can be reported.

As with soluble-insoluble reactions, soluble-soluble reactions are considered electrochemically reversible if the peak position is independent of scan rate and the peak height is linear with the square root of scan rate. For a reversible, soluble-soluble reaction, the Randles-Ševčík relationship is typically used as written in Eq. 5 [35–37]:

$$I_p = 0.4463AC_o^*\sqrt{D_o\frac{n^3F^3}{RT}v}\,. \tag{5}$$

2.2.5 Chronoamperometry (CA)

CA was also used to calculate the diffusivity of the analyte species. CA was performed by applying potentials to quickly reach the mass transfer limiting current before surface area growth on the electrode could significantly augment the current response. The Cottrel equation, shown in Eq. 6, can be used to calculate the diffusivity from the current response in the mass transfer limiting region [35, 38]:

$$I = \frac{nFAC_o^*\sqrt{D_o}}{\sqrt{\pi t}}\,, \tag{6}$$

where I represents current, t represents time, and all other variables are as previously defined. Six to nine CA measurements were taken in each system by applying sufficiently negative potentials for 3 seconds, followed by 60 seconds at a sufficiently positive potential to clean the electrode.

2.2.6 Chronopotentiometry (CP)

CP was used as an additional means to calculate the diffusivity of the analyte species. CP experiments were conducted by applying a sufficiently positive potential to clean the electrode for 60 seconds before applying a negative sufficient to induce the deposition reaction of interest. When the diffusion layer grows large enough with time, the applied current can no longer be met by the reaction of interest, and the potential will quickly change to initiate additional reactions to meet the current demanded by the power supply. The time needed for the sudden change (or transition) in potential to occur is referred to as the transition time, τ, and can be related to diffusivity by the Sand equation [39], shown in Eq. 7:

$$\frac{I\tau^{0.5}}{C_O^*} = \frac{nFA\sqrt{D_O\pi}}{2}, \quad (7)$$

where all variables are as previously defined. This relationship holds as long as the left side of the equation remains constant, therefore as $\tau^{0.5}$ changes, current changes inversely. Practical issues such as double-layer charging, surface area growth, and secondary reactions can interfere with the precise definition and calculation of transition time [40]. Several simple graphical methods have been proposed for the measurement of transition time. A previous study showed that the Kuwana method is the most accurate and precise of the evaluated methods [41]. The Kuwana method is used by simply finding the point during the transition of interest where the CP curve becomes straight after the sudden change in potential (referred to as the transition point). The transition time is equal to the amount of time elapsed from the moment of applying current to the transition point. Five CP measurements were taken in each salt system.

2.2.7 Open-circuit potential (OCP)

OCP was recorded to quantify the standard redox potential for the analyte species. OCP measurements were conducted directly after CP measurements by allowing the system to relax until the change in WE potential was less than 1 μV s^{-1} (i.e., $dV/dt < 1 \times 10^{-6}$ V/s) for 10 data points (1 sec). The OCP value for each measurement was calculated by averaging the last 10 data points. For each analyte species, four or five OCP measurements were taken and averaged. The form of the Nernst equation shown in Eq. 8 was used to calculate the standard apparent redox potential for the Sn^{2+}/Sn couple versus the 5 mol% Ag/AgCl RE:

$$E = E^{0\prime} + \frac{RT}{nF}\ln\left(\frac{C_{M^{n+}}}{C^0}\right), \quad (8)$$

where E is the average OCP value, $E^{0\prime}$ is the standard apparent reduction potential, $C_{M^{n+}}$ is the concentration of Sn^{2+} in the bulk salt in units of molarity, molality, or mole fraction, C^0 is the standard concentration matching the units used in the bulk concentration (i.e., 1 M, 1 m, or 1, respectively), and all other variables are the same as previously defined. Eq. 8 assumes an infinite dilution standard state when using molarity or molality [42] and pure standard state when using mole fraction.

For a more detailed review of these and other electrochemical methods, seek other published materials [35, 40]. Error is reported along with calculated values. Error is calculated according to accepted statistical methods that can be found in any standard statistics textbook [43].

2.3 Chemical Analysis

An Inductively Coupled Plasma Mass Spectrometer (ICP-MS, Agilent 7900) was used for quantitative concentration analysis for each experiment. Approximately 1 g of total salt was taken from each salt sample. All salt samples were digested in about 25 g of diluted 18 wt.%

trace metals grade HNO_3 (67-70 wt.% Omnitrace Nitric Acid, Sigma-Aldrich, NX0407-4) in "ultra-clean" plastic containers. Ultra-clean plastic containers were cleaned prior to use three times with Alconox, DI water, and ultra-pure filtered water (18.2 MΩ). HNO_3 was diluted with ultra-pure water in ultra-clean containers. After complete digestion of samples was observed, each sample solution was filtered through 0.45 µm filters and diluted to acquire bulk solutions of <2000 ppm salt concentration. Samples were diluted by mass with 2 wt.% HNO_3. Sn, Ni, and Cu standards were prepared by Inorganic Ventures and purchased from Texas Scientific Products. All standards were diluted by mass using 2 wt.% HNO_3.

The standard addition method was used to separate each dissolved salt sample into 5 calibration aliquots with the amount of standard varying linearly from 0-2 g of mixed Sn-Ni or Sn-Cu standard. The mixed standard was prepared to match the expected sample concentration ranges of Sn, Cu, and Ni respectively. The counts per second recorded by the mass spectrometer were converted into concentrations (ppm) with their associated error using Eq. 9 [44]:

$$C_x = \frac{bC_s}{mV_x}, \tag{9}$$

where C_x is the concentration of the sample, C_s is the concentration of the standard, b is the y-intercept of the linear least-squares line, m is the slope of the linear least-squares line, and V_x is the volume of calibration aliquot containing the dissolved sample. Error was calculated using Eq. 10 [44]:

$$s_v = \frac{s_y}{m}\sqrt{\frac{1}{N} + \frac{(0-\bar{y})^2}{m^2 S_{xx}}}, \tag{10}$$

where s_v is the standard deviation in volume, s_y is the standard deviation about regression, m is the slope of the linear least-squares line, N is the number of points in the calibration curve, $\bar{y}$ is the mean value of the calibration results, and S_{xx} is the sum of the squares of the deviations of x values from the mean. The concentration of each analyte was converted from weight fraction to mol cm^{-3} using a eutectic salt density of 1.713 g cm^{-3}, as calculated previously by Chipman et al [27]. Concentrations for each analyte are reported with their associated error for each experiment in Table 1.

Table 1: Concentration of analyte in each salt sample quantified by ICP-MS.

Analyte(s)	Temperature (K)	Sn^{2+} Concentration (10^{-5} mol cm^{-3})	Ni^{2+} Concentration (10^{-5} mol cm^{-3})	Cu^{+} Concentration (10^{-5} mol cm^{-3})
Sn^{2+}	685	6.501 ± 0.448	--	--
Sn^{2+}	683-788	1.793 ± 0.120	--	--
Ni^{2+}	687	--	*5.893 ± 0.022	--
Ni^{2+} (w/ Sn^{2+})	685	*6.095 ± 0.015	6.847 ± 0.379	--
Cu^{+} (w/ Sn^{2+})	683	1.793 ± 0.120	--	2.791 ± 0.991

*Value based on process knowledge

3.0 Results and Discussion

3.1 Peak Identification

The section details the peak pairs (the oxidation and corresponding reduction peaks) present in CV measurements for each analyte combination studied (i.e., $SnCl_2$ only, $NiCl_2$ only, $SnCl_2$ and $NiCl_2$, $SnCl_2$ and CuCl). It also provides the rationale for the assignment of redox reactions responsible for peak pairs. In general, assignment of redox reactions to the peak pairs in CV measurements are based on the characteristic shape of the peaks, calculated *n* from SWV measurements, and estimated $E^{0\prime}$values from previous publications in LiCl−KCl eutectic and/or thermochemical data, as shown in Table 2. Based on the observed location of peaks in the following CV plots, an equilibrium potential was approximated and compared to the estimated $E^{0\prime}$. The values of $E^{0\prime}$ provide an expected order in which peaks will appear and approximate location. $E^{0\prime}$ values do not account for concentration effects, which can be as much as ±0.22 V based on Eq. 8 and the concentrations in Table 1.

Table 2: Summary of peak pair reaction assignments, electron transferred calculations from SWV, and estimated $E^{0\prime}$ from LiCl−KCl data for specified signal peak pairs.

Peak Pair	Half-Cell Reaction	n calculated from SWV	Approximate E_{eq} / V vs. 5 mol% Ag/AgCl	Estimated $E^{o\prime}$ / V vs. Theoretical Ag/AgCl (5 mol%)[1]
A/A'	$Cl_2 + 2e^- \leftrightarrow 2Cl^-$	--	1.15 V	1.04 V
B/B'	$Sn^{4+} + 2e^- \leftrightarrow Sn^{2+}$	--	0.35 V	0.33 V[2]
C/C'	$Sn^{2+} + 2e^- \leftrightarrow Sn$	1.84 ± 0.14	−0.45 V	−0.34 V
D/D', E/E', F/F', G/G'	Sn-Li and Sn-Ca alloys	--	−1.85 to −2.45	--
H/H'	$Li^+ + e^- \leftrightarrow Li$ and/or $Ca^{2+} + 2e^- \leftrightarrow Ca$	--	−2.60 V	−2.58 V (Li^+/Li) −2.53 V (Ca^{2+}/Ca)[2]
I/I'	$Ni^{2+} + 2e^- \leftrightarrow Ni$	1.55 ± 0.08	−0.15 V	−0.06 V
J/J'	Sn-Ni alloy	--	−0.35 V	--
K/K'	Ni-Ca alloy	--	−1.85 to −2.45	--
L/L'	$Cu^{2+} + e^- \leftrightarrow Cu^+$	0.91 ± 0.06	0.80 V	0.78 V
M/M'	$Cu^+ + e^- \leftrightarrow Cu$	--	−0.40 V	−0.20 V
N/N'	Sn-Cu alloy	--	−0.43 V	--
P/P'	Cu-Li or Cu-Ca alloy	--	−1.85 to −2.45	--

[1] $E^{o\prime}$ values are taken from Plambeck [45] at 723K in LiCl-KCl on molality basis and adjusted to a theoretical Ag/AgCl(5 mol%) scale by subtracting -0.738 V. The theoretical Ag/AgCl(5 mol%) was calculated using E^o(Ag/AgCl) on molality basis of -0.727 V in the Nernst Equation ($E = E^o + RT/Fln(0.833) = -0.738\,V$). 5 mol% is approx. 0.833 molal in LiCl-KCl eutectic. [2]Estimated from thermochemical data by Barin [46] using method published by Zhang [47].

3.1.1 $SnCl_2$ in LiCl−KCl−$CaCl_2$

The full electrochemical window of the LiCl–KCl–$CaCl_2$ system with dilute $SnCl_2$ is shown in Figure 2. The A/A' signal pair at the upper limit of the window corresponds to the Cl_2/Cl^- redox couple [22, 23]. The H/H' signal pair at the lower limit of the window corresponds to either the Li^+/Li redox pair, the Ca^{2+}/Ca redox pair, or the co-deposition of Ca and Li [22, 23, 48]. The G/G', F/F', E/E', and D/D' signal pairs are attributed to different alloys of Sn with Li and Ca (e.g., Li_2Sn_5, LiSn, $CaSn_3$) [11, 49–51], but the authors are unaware of any study that conclusively determines their respective compositions. The sharp rise and fall of these peaks are consistent with reactions constrained by the availability of reactants on the surface of the WE. Notably 4 distinct anodic peaks appear for the Sn alloys, which is one more anodic peak than those previous identified to be associated with Sn-Li alloys in LiCl–KCl and LiCl melts [11, 49]. Hence, a Sn-Ca alloy may be responsible for the additional anodic peak among peaks G, F, E and D. Because of the abundance of Sn-Li and Sn-Ca alloys [50, 51], alloy compositions will not be considered further in this study. The C/C' signal pair is attributed to the Sn^{2+}/Sn redox pair, which is the primary focus of this study and will be discussed in detail below. The B/B' signal pair is attributed to the Sn^{4+}/Sn^{2+} redox pair and will be considered and discussed separately.

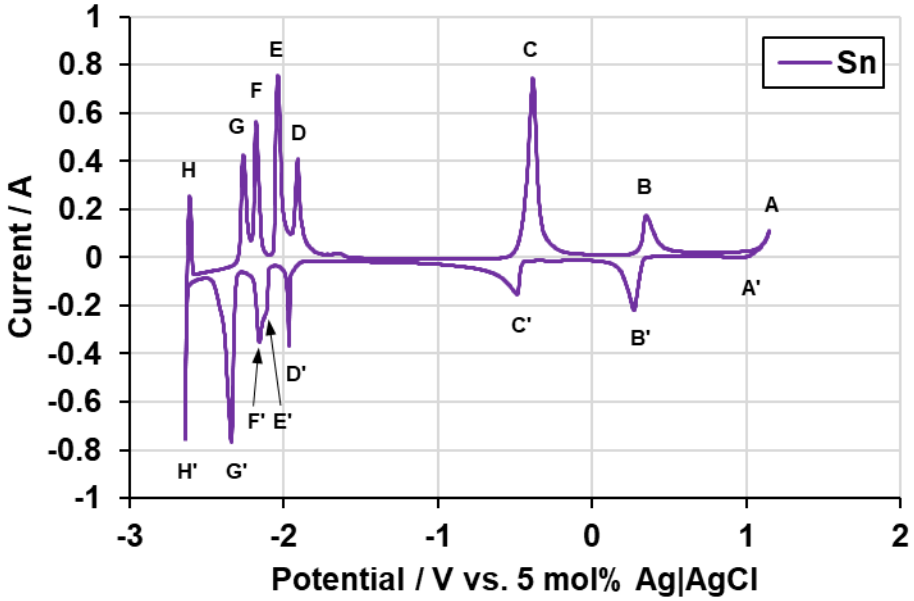

Figure 2: Full electrochemical window scan of $SnCl_2$ (6.5×10^{-5} mol cm^{-3}) in LiCl-KCl-$CaCl_2$ eutectic. WE: 1.5 mm W rod (0.812 cm^2), CE: 3.175 mm W rod, RE: 5 mol% Ag/AgCl, Temperature: 685 K, 88% IR compensation (0.22/0.25 Ω), scan rate: 0.1 V/s.

SWV measurements were conducted to support the peak assignment of the C/C' signal pairs by calculating the number of electrons exchanged in the reaction. Figure 3 shows SWV profiles for several frequencies for the C' peak. The asymmetric peaks represented in Figure 3 demonstrate the typical SWV profile of a soluble-insoluble redox reaction (i.e., Sn^{2+}/Sn) [29]. The average n value for the Sn^{2+}/Sn reaction was calculated to be 1.84 ± 0.14 using Eq 1. The assignment of the Sn^{4+}/Sn^{2+} redox pair is implied by the confirmation of the Sn^{2+}/Sn pair and evidence from previous studies [3, 11]. Peak assignments and average calculated n values are summarized in Table 2.

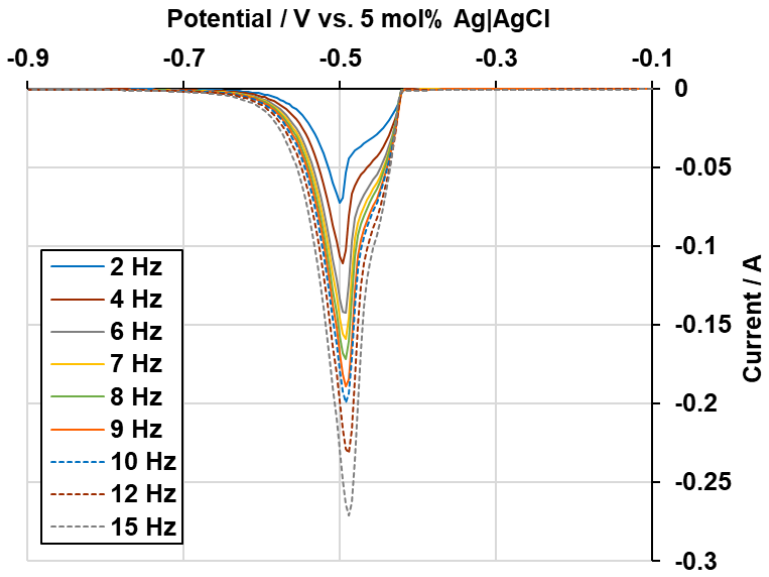

Figure 3: SWV in LiCl-KCl-$CaCl_2$ eutectic for Sn reduction peak from the $SnCl_2$ (6.5 x 10^{-5} mol cm^{-3}) system. WE: 1.5 mm W rod (0.812 cm^2), CE: 3.175 mm W rod, RE: 5 mol% Ag/AgCl, Temperature: 685 K, 88% IR compensation (0.22/0.25 Ω); step: -0.004 V, amplitude: 0.05 V.

3.1.2 $NiCl_2$ in LiCl–KCl–$CaCl_2$

The full electrochemical window of dilute $NiCl_2$ in the LiCl-KCl-$CaCl_2$ system is shown in Figure 4. The I/I' signal pair is attributed to the Ni^{2+}/Ni redox pair, as the only substantial signal peak in the window [3, 52]. The shape of the I/I' peak pair is consistent with a deposition reaction. The behavior and characteristics of the Ni^{2+}/Ni reaction pair are discussed below.

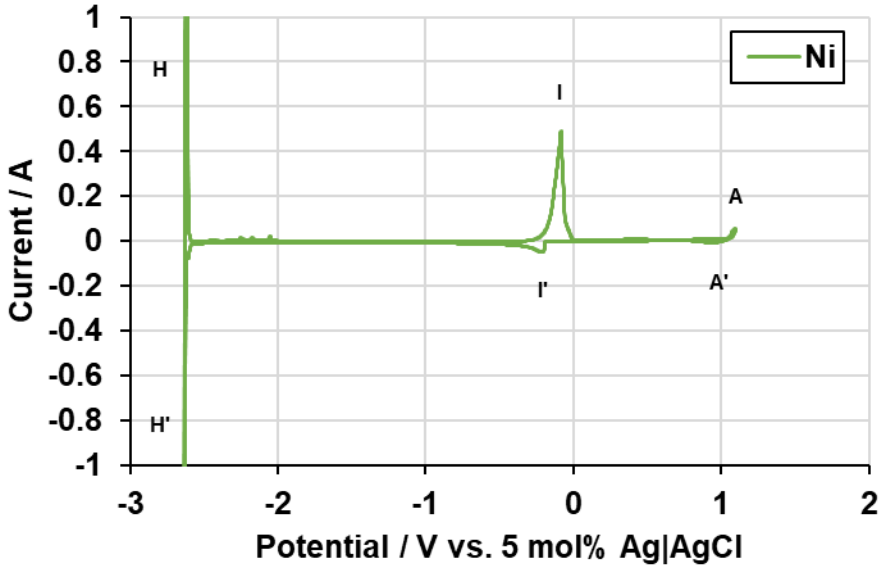

Figure 4: Full electrochemical window scan of $NiCl_2$ (5.9 x 10^{-5} mol cm^{-3}) in LiCl-KCl-$CaCl_2$ eutectic. WE: 1.5 mm W rod (0.675 cm^2), CE: 3.175 mm W rod, RE: 5 mol% Ag/AgCl, Temperature: 687 K, 91% IR compensation (0.25/0.275 Ω), scan rate: 0.1 V/s.

SWV measurements were conducted to support the peak assignment of the I/I' signal pair by calculating the number of electrons exchanged in the reaction. Figure 5 shows SWV profiles for several frequencies for the I' peak. The asymmetric peaks represented in Figure 5 demonstrate the typical SWV profile of a soluble-insoluble redox reaction (i.e., Ni^{2+}/Ni) [29]. The average n value for the Ni^{2+}/Ni reaction was calculated to be 1.55 ± 0.08 using Eq. 1. Peak assignments and average calculated n values are summarized in Table 2.

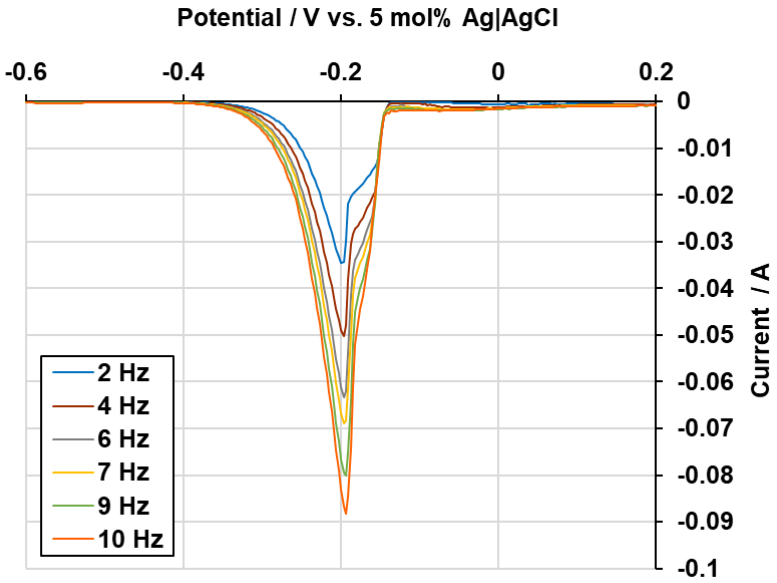

Figure 5: SWV in LiCl-KCl-$CaCl_2$ eutectic for Ni deposition peak from the $NiCl_2$ (5.9×10^{-5} mol cm^{-3}) system. WE: 1.5 mm W rod (0.675 cm^2), CE: 3.175 mm W rod, RE: 5 mol% Ag/AgCl, Temperature: 687 K, 91% IR compensation (0.25/0.275 Ω); step: -0.003 V, amplitude: 0.05 V.

3.1.3 $SnCl_2$-$NiCl_2$ in LiCl–KCl–$CaCl_2$

Two unique peaks were identified with the mixed $SnCl_2$-$NiCl_2$ system, as shown in Figure 6. The K/K' signal pair may be attributed to a Sn-Ni-Ca alloy since the Ni-Ca, Sn-Ni, and Sn-Ca phase diagrams each indicate several intermetallic compounds [51, 53, 54]. The J/J' signal pair is attributed to the formation of a Ni-Sn alloy, which is most likely Ni_3Sn_4 since its phase borders the other side of the two-phase region by liquid Sn below 798 K [53]. However, the intermetallic compound forms depending on several parameters, such as temperature, applied potential, time of electrolysis, and the concentration ratio between Sn^{2+}/Ni^{2+} [3, 55].

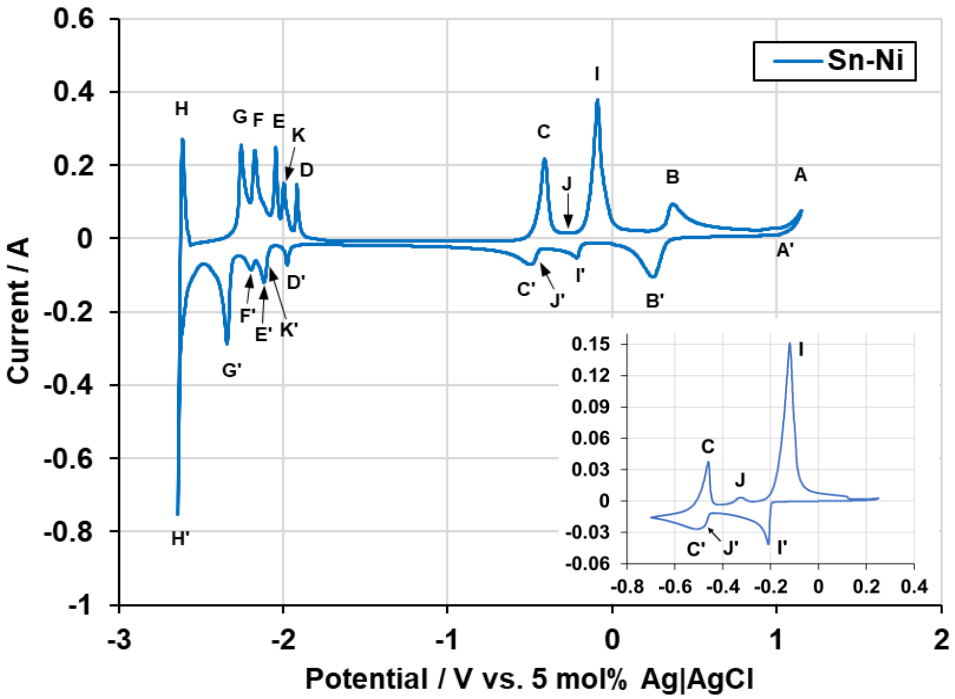

Figure 6: Full electrochemical window scan of $SnCl_2$(6.1 x 10^{-5} mol cm^{-3})-$NiCl_2$(6.8 x 10^{-5} mol cm^{-3}) in LiCl-KCl-$CaCl_2$ eutectic. WE: 1.5 mm W rod (0.506 cm^2), CE: 3.175 mm W rod, RE: 5 mol% Ag/AgCl, Temperature: 685 K, 94% IR compensation (0.37/0.395 Ω), scan rate: 0.1 V/s; Insert: scan range: -0.7 V to 0.25 V.

The J' signal is indistinguishable from the C' signal in Figure 6. Hence, the Ni-Sn alloy may simply form between Sn and Ni deposits on the WE explaining the lack of a distinguishable J' signal. Alternatively, the reduction potential for forming Sn-Ni alloy may be slightly more positive than Sn deposition. The proximity of their reduction potentials and peak broadening effect of ion diffusion could make the C' and J' signals indistinguishable from one another. However, the C and J oxidation peaks are more distinguishable due to the metals and alloys being on the surface of the electrode resulting in a sharper rise and fall. The behavior of the mixed Sn^{2+}/Ni^{2+} system is further considered in subsequent sections.

3.1.4 $SnCl_2$-CuCl in LiCl–KCl–$CaCl_2$

Four unique peaks were identified with the mixed $SnCl_2$-CuCl system, as shown in Figure 7. The P/P' signal pair is attributed to a Cu-Li solution or Cu-Ca alloy since the Cu-Li phase diagram indicates a high solubility of Li in solid Cu and the Cu-Ca phase diagram indicates several intermetallic compounds [56, 57]. The N/N' signal pair, located between the M/M' and C/C' signal pairs is quite indistinct, but is likely the response of a Cu-Sn alloy of unknown composition [58]. The L/L' signal pair is attributed to the Cu^{2+}/Cu^{+} pair due to its shallow peak heights, typical of an electrochemically reversible, soluble-soluble, single electron exchange reaction [59]. The M/M' signal pair is attributed to the Cu^{+}/Cu redox pair based on its more positive $E^{0\prime}$ value relative to Sn^{2+}/Sn (see Table 2) [60, 61].

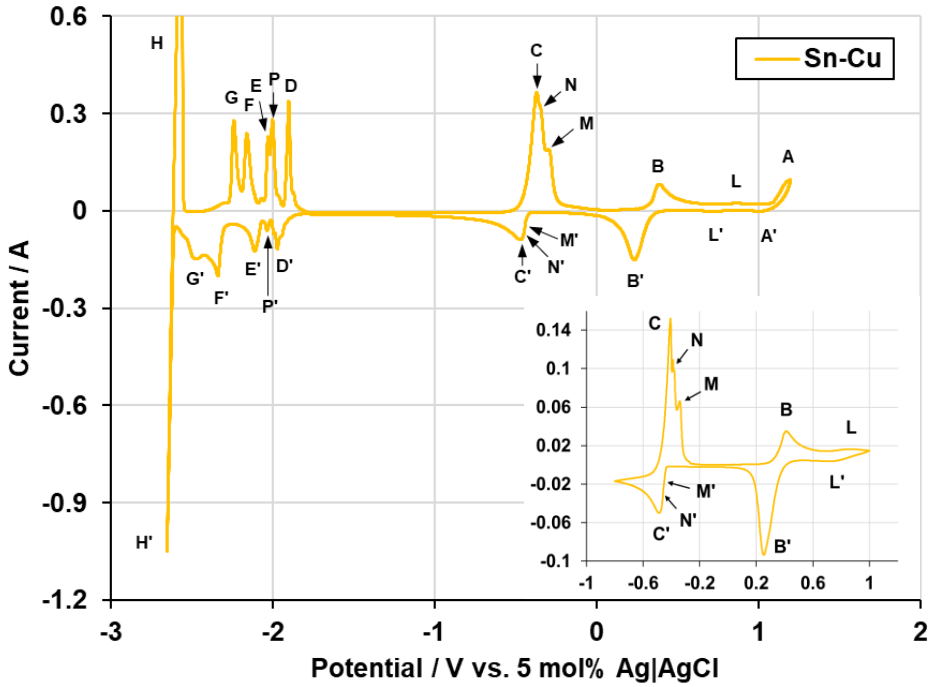

Figure 7: Full electrochemical window scan of $SnCl_2$(1.8 x 10^{-5} mol cm^{-3})-CuCl(2.8 x 10^{-5} mol cm^{-3}) in LiCl-KCl-$CaCl_2$ eutectic. WE: 1.5 mm W rod (1.38 cm^2), CE: 3.175 mm W rod, RE: 5 mol% Ag/AgCl, Temperature: 683 K, 78% IR compensation (0.14/0.18 Ω), scan rate: 0.1 V/s; Insert: scan range: -0.8 V to 1 V.

The M' and N' signals are indistinguishable in Figure 7 for the same reasons discussed for J' in Figure 6—alloy formation upon deposition of Sn on deposited Cu, similar reduction potentials, and/or broader reduction peaks. Based on CV measurements over -0.2 to -0.8 V, a clear shoulder emerges for N' and/or M', as shown later. This indicates that a Cu electrodeposition occurs initially and is closely followed by Sn deposition. The presence of the N signal likely indicates that a Sn-Cu alloy forms. Distinct features appear for M and N appear during oxidation due to the sharp oxidation peak shape of surface constrained metals and alloys. The behavior of the mixed Sn^{2+}/Cu^{+} system is further considered in subsequent sections.

SWV measurements were conducted to support the peak assignments of the L/L' and M/M' signal pairs by calculating the number of electrons exchanged in each reaction. Figure 8 shows SWV profiles for several frequencies for the L' peak. SWV could not be performed on the M' peak because of the proximity of the C' and N' peaks. The symmetric peaks represented in Figure 8 demonstrate the typical SWV profile of a soluble-soluble redox reaction (Cu^{2+}/Cu^{+}). The average n value for the Cu^{2+}/Cu^{+} reaction was calculated to be 0.91 ± 0.06 using Eq 2. The attribution of the Cu^{+}/Cu redox pair for M/M' is implied by the confirmation of the Cu^{2+}/Cu^{+} pair. Peak assignments and average calculated n values are summarized in Table 2.

CuCl, as an isolated analyte, was not examined in this study. Observing the close proximity of reduction signals for Sn and Cu electrodeposition revealed that Cu would pose a significant challenge as an impurity during electrochemical purification of Sn in LiCl–KCl–$CaCl_2$. Effective separation of Cu from Sn would likely require an alternative electrolyte or separation scheme. Consequently, further investigation of CuCl electrochemistry in LiCl–KCl–$CaCl_2$ offered limited practical value and was not pursued.

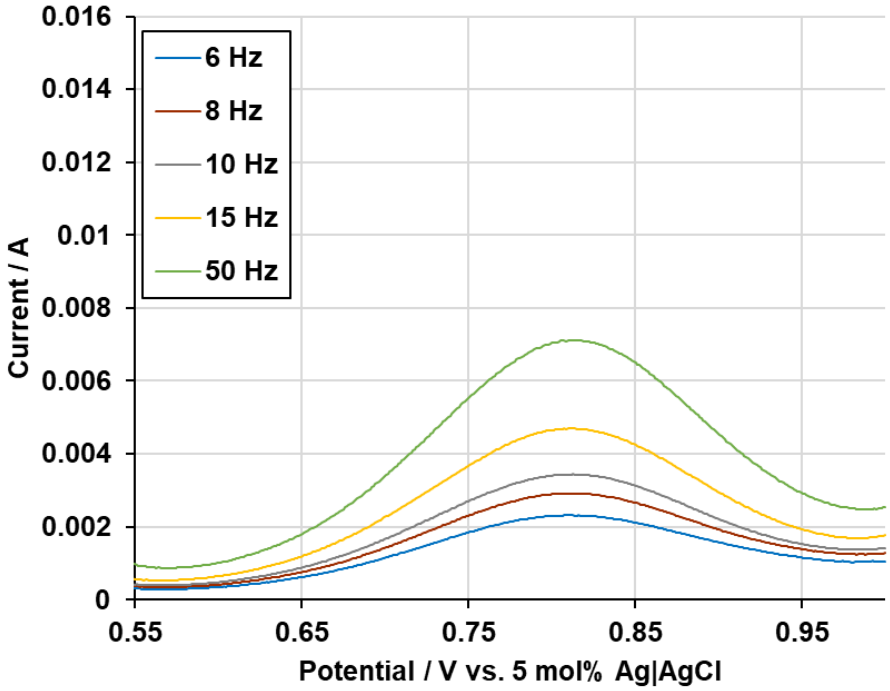

Figure 8: SWV in LiCl-KCl-$CaCl_2$ eutectic for Cu^+ oxidation peak from the $SnCl_2$(1.8×10^{-5} mol cm^{-3})-CuCl(2.8×10^{-5} mol cm^{-3}) system. WE: 1.5 mm W rod (1.38 cm^2), CE: 3.175 mm W rod, RE: 5 mol% Ag/AgCl, Temperature: 683K, 78% IR compensation (0.14/0.18 Ω); step: 0.001 V, amplitude: 0.02 V.

3.2 Cyclic Voltammetry

CV was conducted to calculate the diffusivities of Sn^{2+} and Ni^{2+} in LiCl-KCl-$CaCl_2$ eutectic salt and Ni^{2+} with dilute $SnCl_2$ in LiCl-KCl-$CaCl_2$. Due to the proximity of the Sn and Cu deposition peaks, analysis was not performed to calculate diffusivity for Cu^+ in LiCl-KCl-$CaCl_2$. Figures 9, 10, 11, and 12 show example CV curves at different scan rates from each salt system. The Sn, Ni, and Cu redox pairs shown all share the sharp peaks typical of a surface constrained deposition reaction.

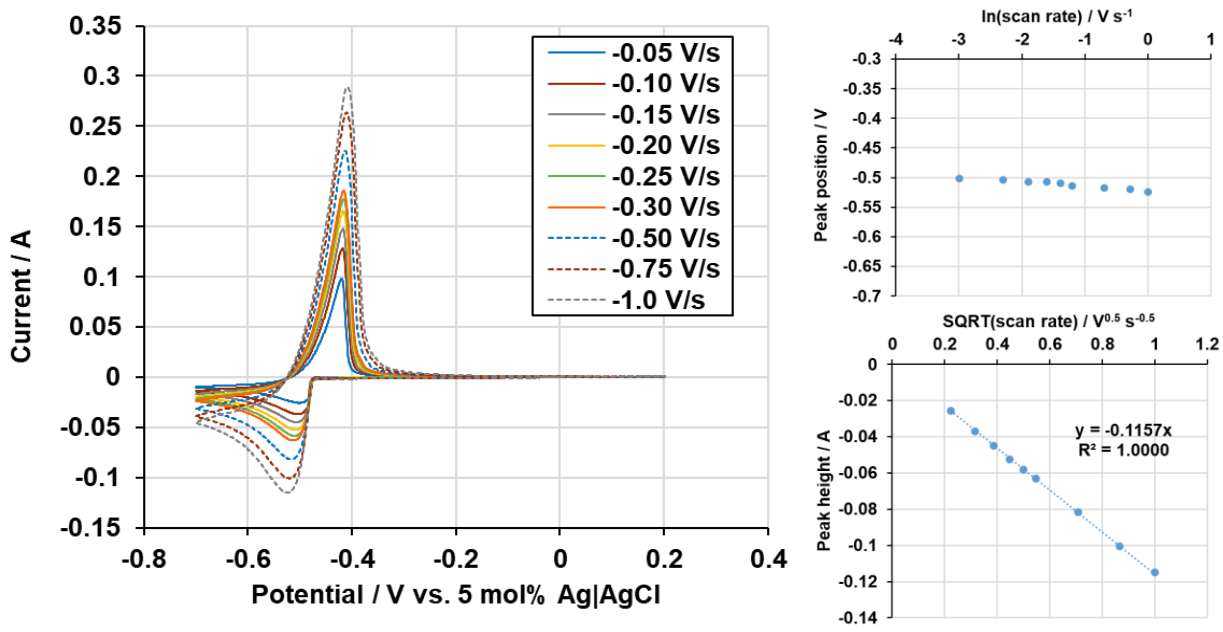

Figure 9: CV in LiCl-KCl-$CaCl_2$ eutectic salt for Sn reduction at various scan rates from the $SnCl_2$ (6.5 x 10^{-5} mol cm^{-3}) system. WE: 1.5 mm W rod (0.812 cm^2), CE: 3.175 mm W rod, RE: 5 mol% Ag/AgCl, Temperature: 685 K, 88% IR compensation (0.22/0.25 Ω).

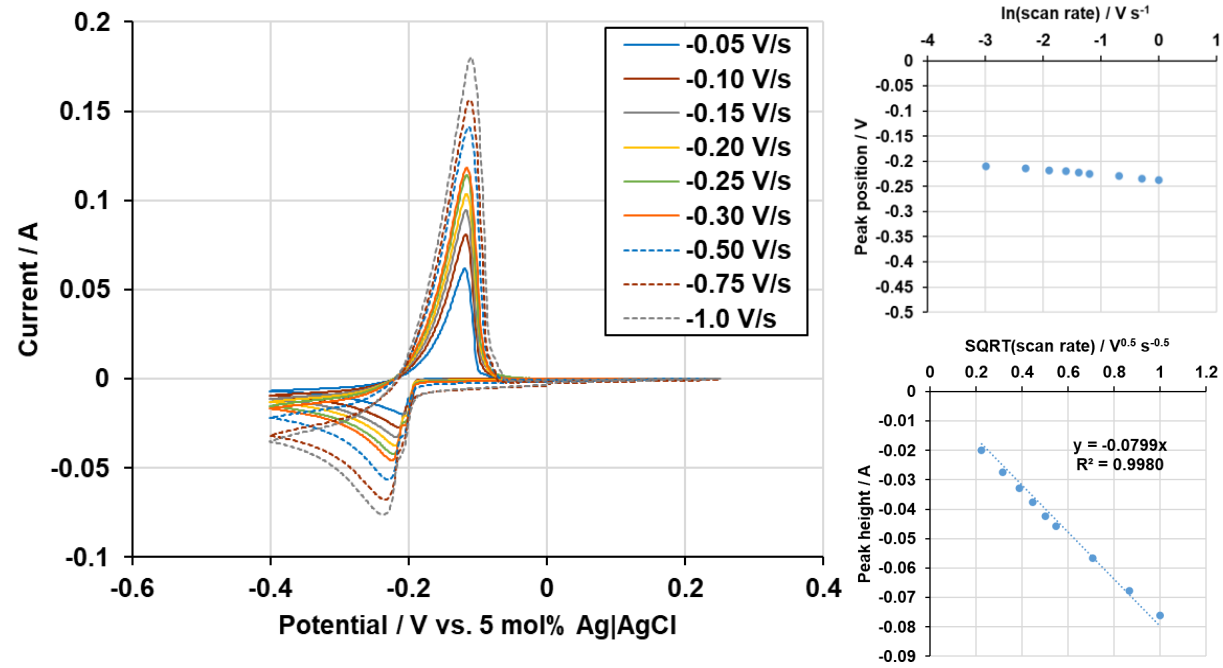

Figure 10: CV in LiCl-KCl-$CaCl_2$ eutectic salt for Ni deposition at various scan rates from the $NiCl_2$ (5.9 x 10^{-5} mol cm^{-3}) system. WE: 1.5 mm W rod (0.675 cm^2), CE: 3.175 mm W rod, RE: 5 mol% Ag/AgCl, Temperature: 687 K, 91% IR compensation (0.25/0.275 Ω).

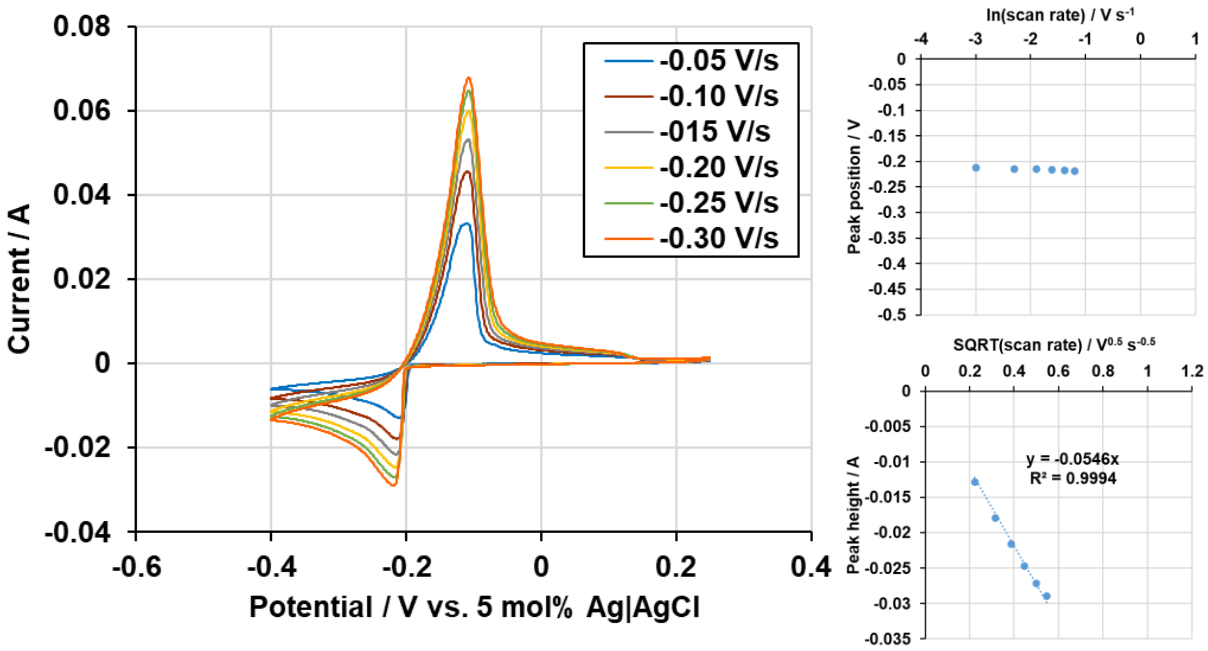

Figure 11: CV in LiCl-KCl-$CaCl_2$ eutectic salt for Ni deposition at various scan rates from the $SnCl_2$(6.1 x 10^{-5} mol cm^{-3})-$NiCl_2$(6.8 x 10^{-5} mol cm^{-3}) system. WE: 1.5 mm W rod (0.506 cm^2), CE: 3.175 mm W rod, RE: 5 mol% Ag/AgCl, Temperature: 685 K, 94% IR compensation (0.37/0.395 Ω).

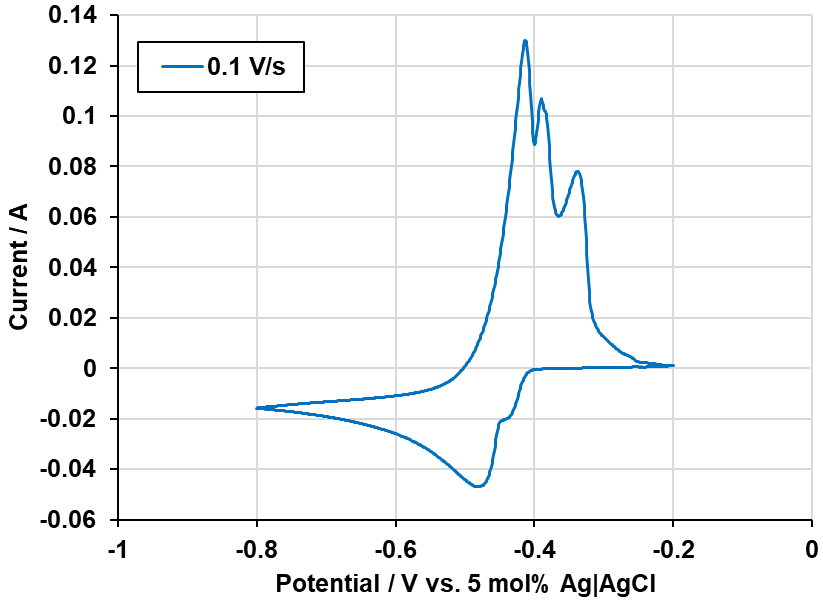

Figure 12: CV in LiCl-KCl-$CaCl_2$ eutectic for Sn and Cu deposition at 0.1 V/s from the $SnCl_2$(1.8 x 10^{-5} mol cm^{-3})-CuCl(2.8 x 10^{-5} mol cm^{-3}) system. WE: 1.5 mm W rod (1.38 cm^2), CE: 3.175 mm W rod, RE: 5 mol% Ag/AgCl, Temperature: 683 K, 78% IR compensation (0.14/0.18 Ω).

In Figure 12, a clear shoulder emerges for N' and/or M', which was not visible in the full electrochemical window in Figure 7. As mentioned earlier, the shoulder starting at -0.41 V indicates that Cu electrodeposition occurs first, followed by Sn-Cu alloy formation, and then Sn electrodeposition. No distinct reduction feature is observed for Sn-Cu alloy formation. However, the triplet of oxidation peaks in Figure 12 likely corresponds to Sn oxidation (left), Sn-Cu alloy oxidation (middle), and Cu oxidation (right).

A soluble-insoluble reaction, such as Sn, Ni, or Cu deposition, is considered electrochemically reversible if the CV reduction peak position is independent of scan rate and the peak height is linear with the square root of scan rate [30, 33]. The minimal shift in peak position with varying scan rates indicates the reaction is electrochemically reversible, as linearity of peak height with square root of scan rate is maintained for both reversible and irreversible reactions, but not for quasi-reversible ones.

By graphing peak height versus the square root of scan rate the slope of the line was related to Eq. 3 to calculate diffusivity. The error was found by finding the error of the slope parameter in the regression and propagating that error with the error of the area, concentration, and temperature. Additionally, semi-integrated CV data was used to calculate diffusivity with Eq. 4. The semi-integration technique also enabled quantification of the diffusivity of Sn^{2+} in the mixed $SnCl_2$-$NiCl_2$ system. The values calculated from each method are compared in Table 3.

Table 3: Calculated diffusivities using CV data for Sn^{2+} with and without Ni^{2+} present in LiCl-KCl-$CaCl_2$ and Ni^{2+} with and without Sn^{2+} present in LiCl-KCl-$CaCl_2$.

Species	Temperature (K)	Berzins-Delahay CV Diffusivity (10^{-5} cm^2 s^{-1})	Semi-integrated CV Diffusivity (10^{-5} cm^2 s^{-1})
Sn^{2+}	685	1.02 ± 0.07	1.10 ± 0.08
Ni^{2+}	687	0.86 ± 0.09	0.87 ± 0.04
Ni^{2+} (w/ Sn^{2+})	685	0.53 ± 0.05	0.67 ± 0.05
Sn^{2+} (w/ Ni^{2+})	685	--	0.32 ± 0.01

Diffusivity values for Sn^{2+} show close agreement between the Berzins-Delahay (B-D) and semi-integrated (S-I) methods, but values for the diffusivity of Ni^{2+} differ significantly. This variability and the larger diffusivity for Ni^{2+} obtained by the S-I method can be explained by differences in surface area growth during deposition of Sn and Ni. Sn deposits as a liquid, which naturally spreads to more evenly coat the electrode limiting surface area growth. Conversely, Ni deposits as a solid and is reported to nucleate and grow three-dimensionally on glassy carbon, stainless steel, and tungsten electrodes in low-temperature molten salts [62]. Three-dimensional growth more rapidly increases electrode surface roughness and active area, amplifying current. Because semi-integration accumulates current over time, it is more sensitive to surface area growth than the B-D equation, which uses a single data point. Both methods are impacted by surface area growth, but semi-integration is affected to a greater extent, explaining the inflated diffusivity of Ni^{2+} when the S-I method is used. Therefore, the diffusivity obtained via the B-D equation is considered more accurate under these conditions.

Table 3 also suggests that the diffusivity of Sn^{2+} is three times smaller in the mixed system than in the isolated system. However, this can be partially explained by considering the available active area on the electrode. Some sites on the electrode will be occupied by Ni^{2+} reducing to Ni, decreasing available active electrode area for Sn deposition and, consequently, artificially decreasing the calculated diffusivity. However, this is not likely to explain a three-fold reduction. Hence, it is possible that the presence of $NiCl_2$ affects the diffusivity of Sn^{2+} by increasing the viscosity of the salt and/or altering complex formations. The exact cause(s) for the lower diffusivity for Sn^{2+} in the mixed $NiCl_2$-$SnCl_2$ system is not fully understood.

3.3 Chronoamperometry

CA experiments were conducted as a supplemental means of calculating the diffusivity of Sn^{2+} in LiCl–KCl–$CaCl_2$ eutectic salt and Ni^{2+} with and without dilute $SnCl_2$ in LiCl–KCl–$CaCl_2$. CA could not be performed on the dilute $SnCl_2$-CuCl system due to the overlap of the Sn^{2+}/Sn and Cu^{+}/Cu signals. Figures 13, 14, and 15 show the CA measurements collected for Sn and Ni.

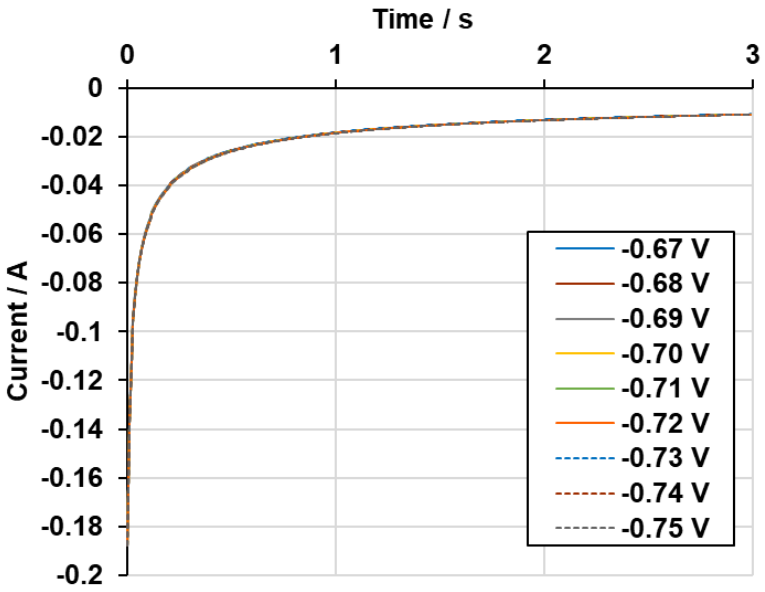

Figure 13: CA in LiCl-KCl-$CaCl_2$ eutectic salt for Sn reduction from the $SnCl_2$ (6.5×10^{-5} mol cm^{-3}) system. WE: 1.5 mm W rod (0.812 cm^2), CE: 3.175 mm W rod, RE: 5 mol% Ag/AgCl, Temperature: 685 K, 88% IR compensation (0.22/0.25 Ω).

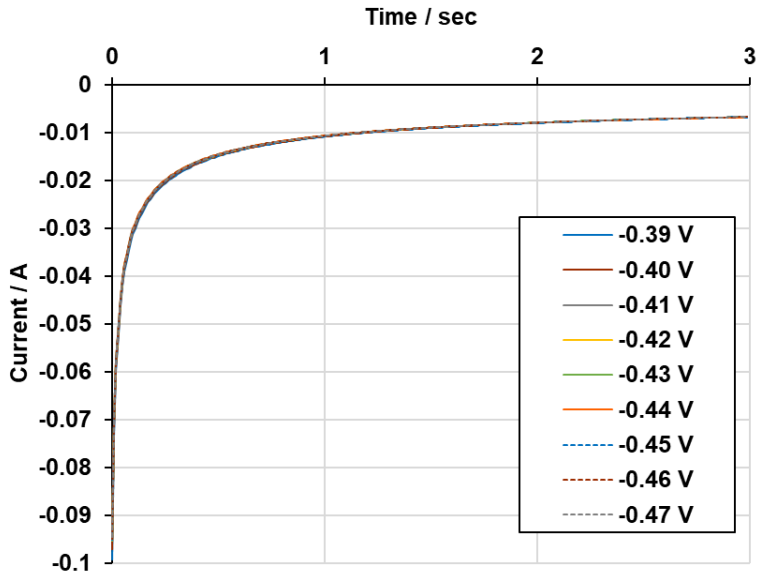

Figure 14: CA in LiCl-KCl-$CaCl_2$ eutectic salt for Ni deposition from the $NiCl_2$ (5.9 x 10^{-5} mol cm^{-3}) system. WE: 1.5 mm W rod (0.675 cm^2), CE: 3.175 mm W rod, RE: 5 mol% Ag/AgCl, Temperature: 687 K, 91% IR compensation (0.25/0.275 Ω).

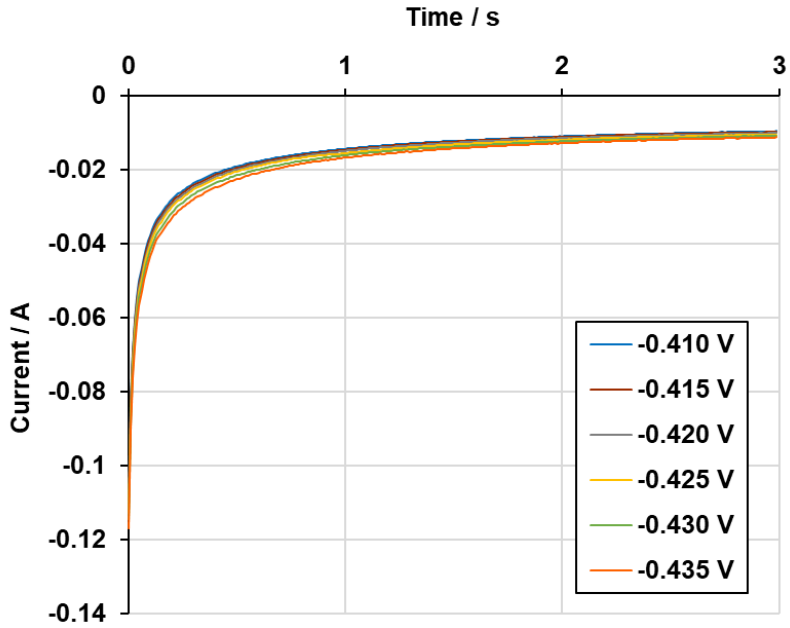

Figure 15: CA in LiCl-KCl-$CaCl_2$ eutectic salt for Ni deposition from the $SnCl_2$ (6.1 x 10^{-5} mol cm^{-3})-$NiCl_2$(6.8 x 10^{-5} mol cm^{-3}) system. WE: 1.5 mm W rod (0.506 cm^2), CE: 3.175 mm W rod, RE: 5 mol% Ag/AgCl, Temperature: 685 K, 94% IR compensation (0.37/0.395 Ω).

Linearizing Eq. 6 demonstrates that the ideal "Cottrellian" region of CA can be found where the slope of the log(I) vs. log(t) data is -0.5 as seen in Eq. 11 [63].

$$\ln I = -0.5 \ln t + \ln \frac{nFAC_O^* \sqrt{D_O}}{\sqrt{\pi}} \qquad (11)$$

A regression of the Cottrellian data can be used to find the y-intercept, which is represented mathematically by the right-most term in Eq. 11. Rearranging and solving this term for D_o yields the diffusivity according to each CA measurement. Error was calculated to include the spread of the CA measurements as a whole and propagated that with errors in the calculated WE area and concentration. Applied potential ranges and analyte diffusivities for each system are reported in Table 4. Significant deviation of the Ni^{2+} diffusivity in the mixed system suggests non-ideal Cottrellian behavior. This is further supported by inconsistent overlap of CA curves as shown in Figure 15.

Table 4: CA potential ranges and average diffusivities for Sn^{2+} in LiCl–KCl–$CaCl_2$ and Ni^{2+} with and without Sn^{2+} present in in LiCl–KCl–$CaCl_2$.

Species	Temperature (K)	Applied Potentials (V)	Average CA Diffusivity (10^{-5} cm^2 s^{-1})
Sn^{2+}	685	-0.67 to -0.75	1.04 ± 0.07
Ni^{2+}	687	-0.39 to -0.47	0.61 ± 0.01
Ni^{2+} (w/ Sn^{2+})	685	-0.410 to -0.435	1.64 ± 0.09

3.4 Chronopotentiometry

CP was also conducted to determine diffusivity of Sn^{2+} in in LiCl–KCl–$CaCl_2$ eutectic salt and Ni^{2+} with and without dilute $SnCl_2$ in LiCl–KCl–$CaCl_2$. CP curves could not be analyzed for the dilute $SnCl_2$–CuCl system due to the overlap of the Sn^{2+}/Sn and Cu^{+}/Cu signals. In this study, the Kuwana method was used to quantify the transition time [41]. The transition point was found by computing the first derivative of the potential data with respect to time. The point in time where the greatest negative change in potential was measured was selected as the transition point. Figures 16, 17, and 18 show example CP measurements from each salt system.

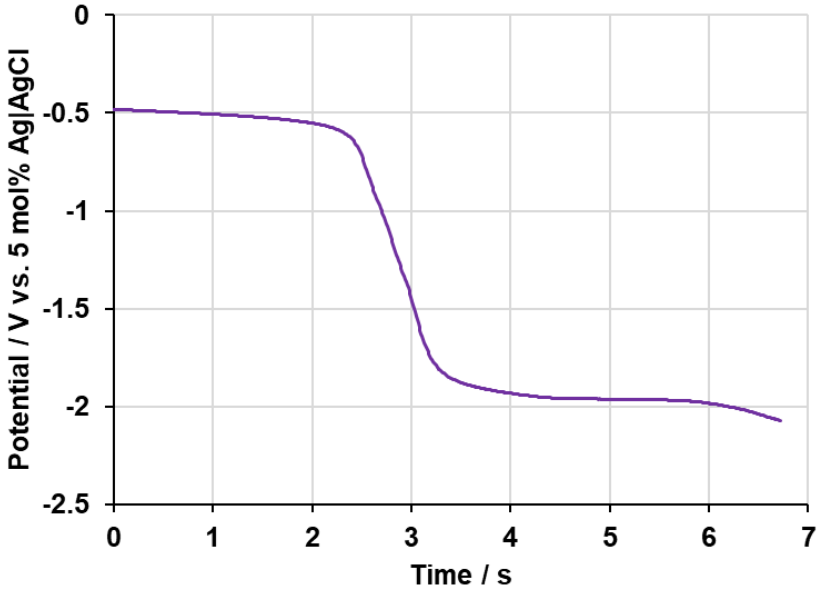

Figure 16: Example CP measurement (-0.019 A) in LiCl-KCl-$CaCl_2$ eutectic salt from the $SnCl_2$ (6.5 x 10^{-5} mol cm^{-3}) system. WE: 1.5 mm W rod (0.812 cm^2), CE: 3.175 mm W rod, RE: 5 mol% Ag/AgCl, Temperature: 685 K.

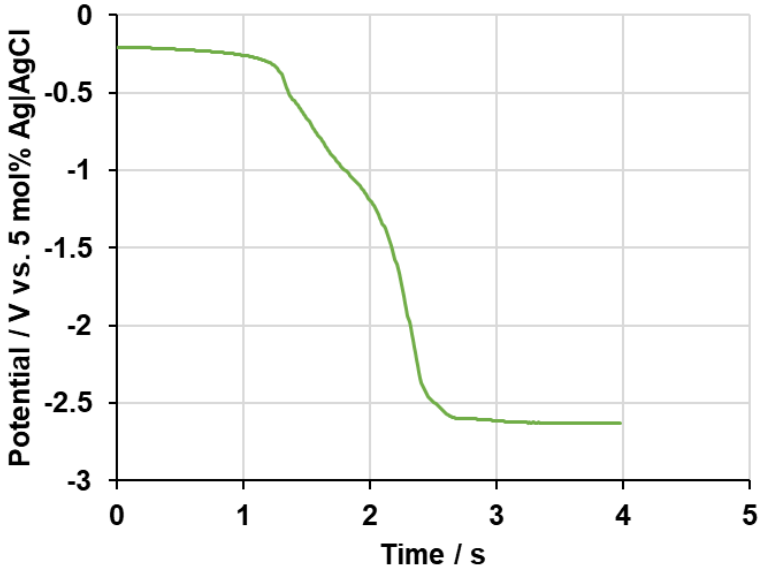

Figure 17: Example CP measurement (-0.016 A) in LiCl-KCl-$CaCl_2$ eutectic salt from the $NiCl_2$ (5.9 x 10^{-5} mol cm^{-3}) system. WE: 1.5 mm W rod (0.675 cm^2), CE: 3.175 mm W rod, RE: 5 mol% Ag/AgCl, Temperature: 687 K.

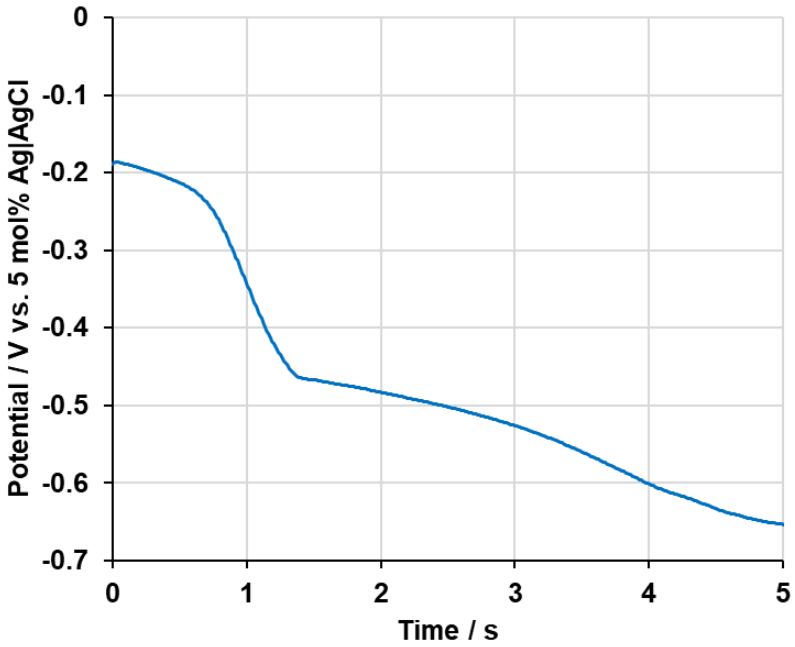

Figure 18: Example CP measurement (-0.018 A) in LiCl-KCl-$CaCl_2$ eutectic salt from the $SnCl_2$ (6.1 x 10^{-5} mol cm^{-3})-$NiCl_2$(6.8 x 10^{-5} mol cm^{-3}) system. WE: 1.5 mm W rod (0.506 cm^2), CE: 3.175 mm W rod, RE: 5 mol% Ag/AgCl, Temperature: 685 K.

The Sand equation (Eq. 7) was used to calculate the analyte diffusivity for each salt system by graphing I vs. $\tau^{-0.5}$ and using the slope to calculate diffusivity. The error was calculated by finding the error of the slope parameter in the regression and propagating that error with the error of the area, concentration, and temperature. Applied currents and diffusivities calculated by CP for each salt system are reported in Table 5. The values calculated using CP predict diffusivities with fairly close agreement with those tabulated above.

Table 5: CP applied current ranges and diffusivities for Sn^{2+} in LiCl–KCl–$CaCl_2$ and Ni^{2+} with and without Sn^{2+} present in LiCl–KCl–$CaCl_2$.

Species	Temperature (K)	Applied Currents (A)	Transition Time (sec)	CP Diffusivity (10^{-5} cm^2 s^{-1})
Sn^{2+}	685	-0.016 to -0.020	2.23 to 3.62	1.14 ± 0.19
Ni^{2+}	687	-0.008 to -0.016	1.33 to 7.71	0.79 ± 0.24
Ni^{2+} (w/ Sn^{2+})	685	-0.015 to -0.019	0.87 to 1.31	0.84 ± 0.39

3.5 Open circuit potential

OCP measurements were conducted to measure the standard apparent redox potential of Sn reduction in LiCl–KCl–$CaCl_2$ eutectic salt versus a 5 mol% Ag/AgCl RE. Figures 19, 20, 21, and 22 depict example OCP measurements that were gathered from each system. Before measuring the OCP, a CP procedure was performed to coat the WE with deposited metal. Occasionally, the potential at the end of the CP would become sufficiently negative for Li and/or Ca to deposit. However, the Li and/or Ca would rapidly exchange with the dissolved analytes (i.e., Sn^{2+}, Ni^{2+}, Cu^{+}) resulting in the sharp rise at the start of the OCP measurements.

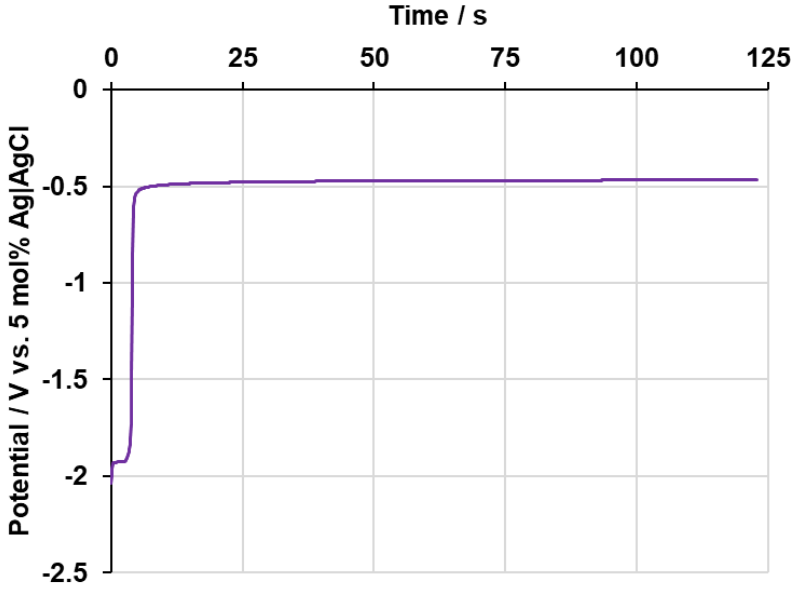

Figure 19: Example OCP data in LiCl-KCl-$CaCl_2$ eutectic salt from the $SnCl_2$ (6.5 x 10^{-5} mol cm^{-3}) system. WE: 1.5 mm W rod (0.812 cm^2), CE: 3.175 mm W rod, RE: 5 mol% Ag/AgCl, Temperature: 685 K.

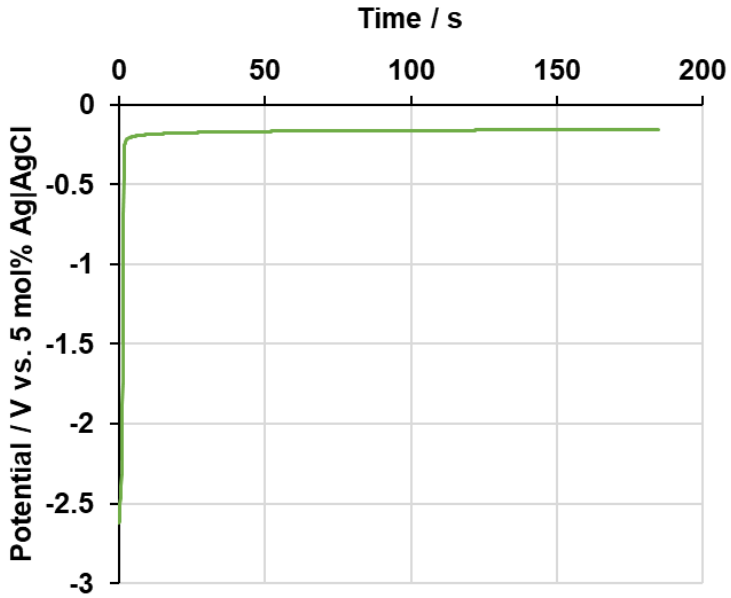

Figure 20: Example OCP data in LiCl-KCl-$CaCl_2$ eutectic salt from $NiCl_2$ (5.9 x 10^{-5} mol cm^{-3}) system. WE: 1.5 mm W rod (0.675 cm^2), CE: 3.175 mm W rod, RE: 5 mol% Ag/AgCl, Temperature: 687 K.

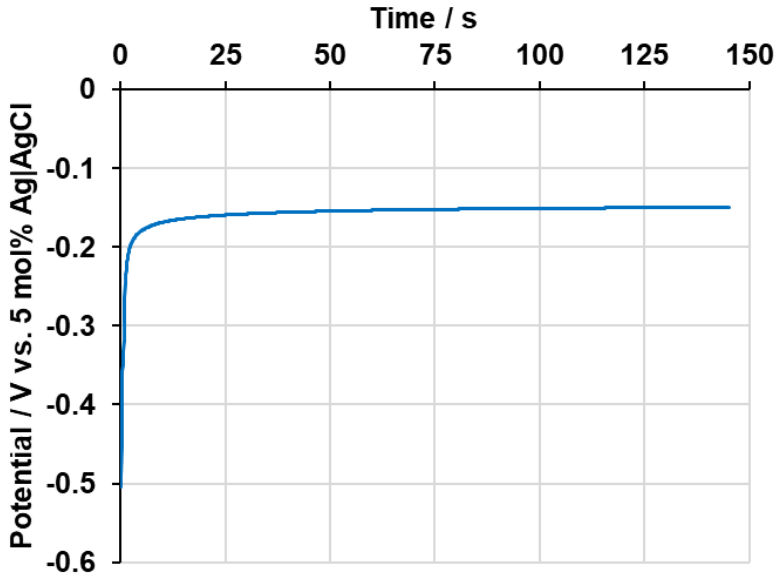

Figure 21: Example OCP data in LiCl-KCl-$CaCl_2$ eutectic salt from the $SnCl_2$ (6.1 x 10^{-5} mol cm^{-3})-$NiCl_2$(6.8 x 10^{-5} mol cm^{-3}) system. WE: 1.5 mm W rod (0.506 cm^2), CE: 3.175 mm W rod, RE: 5 mol% Ag/AgCl, Temperature: 685 K.).

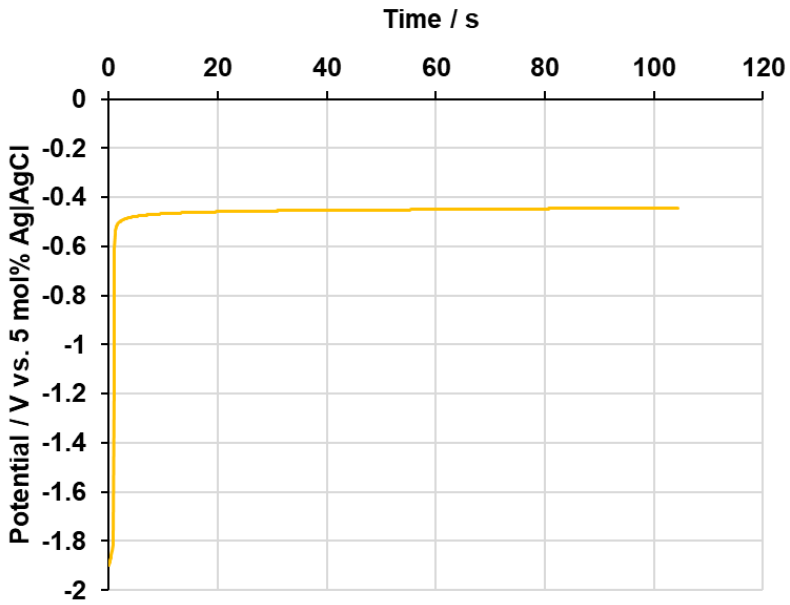

Figure 22: Example OCP data in LiCl-KCl-$CaCl_2$ eutectic salt from the $SnCl_2$(1.8×10^{-5} mol cm^{-3})-CuCl(2.8×10^{-5} mol cm^{-3}) system. WE: 1.5 mm W rod (1.38 cm^2), CE: 3.175 mm W rod, RE: 5 mol% Ag/AgCl, Temperature: 683 K.

The OCP values from each measurement were averaged to determine the average OCP value for each salt system. The reported error for the average OCP value was obtained by taking a 95% confidence interval on all datapoints considered in the average OCP value. Experimentally determined apparent standard reduction potentials are reported in Table 6 using mole fraction ($E_x^{0\prime}$), molality ($E_m^{0\prime}$) and molarity ($E_M^{0\prime}$). The standard apparent potentials are converted to Cl_2 /Cl^- reference potentials (E_x^0, E_m^0, and E_M^0) using the data from Yoon et al. [64]. The errors associated with each apparent standard reduction potential were calculated to include errors in the average OCP value, the temperature value, and the concentration value considering the effect of the natural log.

Table 6: Average OCP values, calculated standard apparent potentials, and standard reduction potentials in LiCl-KCl-$CaCl_2$.

Redox Couple	Sn^{2+}/Sn	Ni^{2+}/Ni	Ni^{2+}/Ni (w/ Sn^{2+})	Cu^{+}/Cu (w/ Sn^{2+})
Temperature / K	685	687	685	683
Average OCP (V vs. 5 mol% Ag/AgCl)	-0.4678 ± 0.0001	-0.1602 ± 0.0009	-0.1497 ± 0.0001	-0.4433 ± 0.0006
$E_x^{0\prime}$ (V vs. 5 mol% Ag/AgCl)	-0.288 ± 0.020	0.022 ± 0.030	0.028 ± 0.020	-0.240 ± 0.046
$E_m^{0\prime}$	-0.371 ± 0.027	-0.061 ± 0.030	-0.055 ± 0.025	-0.322 ± 0.056

(V vs. 5 mol% Ag/AgCl)				
$E_M^{0\prime}$ (V vs. 5 mol% Ag/AgCl)	-0.387 ± 0.029	-0.077 ± 0.030	-0.071 ± 0.027	-0.338 ± 0.060
E_x^0 (V vs. Cl_2/ Cl^-)	-1.330 ± 0.020	-1.019 ± 0.030	-1.013 ± 0.020	-1.281 ± 0.046
E_m^0 (V vs. Cl_2/ Cl^-)	-1.413 ± 0.027	-1.102 ± 0.030	-1.096 ± 0.025	-1.364 ± 0.056
E_M^0 (V vs. Cl_2/ Cl^-)	-1.429 ± 0.039	-1.118 ± 0.030	-1.112 ± 0.027	-1.379 ± 0.060

On a molarity basis, the standard reduction potential ($E_M^{0\prime}$) of -1.429 V calculated for Sn^{2+}/Sn on in eutectic LiCl–KCl–$CaCl_2$ is within 39 mV and 25 mV, respectively, of the values reported by Ghallali et al. (-1.39 V vs Cl_2/ Cl^-at 743 K) [3] and Laitinen and Liu (-1.404 V vs Cl_2/ Cl^-at 723 K) [9] in LiCl–KCl. For the Ni^{2+}/Ni pair, the value of $E_M^{0\prime}$ calculated in this work is within 1 mV and 62mV, respectively, of the values from Laitinen and Liu (-1.117 V vs Cl_2/ Cl^-at 723 K) and Ghallali et al. (-1.18 V vs Cl_2/ Cl^-at 743 K). Because the differences in temperature and the effect of $CaCl_2$ on LiCl–KCl reduction potential is unknown, a more rigorous comparison to prior results cannot be made.

The standard apparent potential values for Cu^+/Cu are within 50 mV of the values for Sn^{2+}/Sn. The proximity of these standard potential values makes it difficult to distinguish between their signals and electrochemically separate Sn from Cu impurities. However, the standard apparent reduction potentials of Ni^{2+}/Ni and Sn^{2+}/Sn are separated by more than 300 mV. Hence, the electrochemical separation of Sn and Ni impurities is more feasible than Sn from Cu impurities. Based on the standard apparent potential values for Ni^{2+}/Ni with and without $SnCl_2$ present, it appears that dilute amounts of $SnCl_2$ have negligible effect on the standard apparent potential of Ni^{2+}/Ni.

3.7 Sn^{4+}/Sn^{2+} Redox Pair

The Sn^{4+}/Sn^{2+} redox reaction was investigated using CV. Castrillejo et al. demonstrated with CV that the Sn^{4+}/Sn^{2+} couple shape corresponds to a soluble-soluble reaction at 723 K in $ZnCl_2$-NaCl molten salts [21]. They also noted that at slower scan rates the absence of the reduction peak indicated Sn^{4+} was quickly lost from the melt by volatilization. This is consistent with the relatively low boiling point of 387 K for $SnCl_4$.

CVs of the Sn^{4+}/Sn^{2+} redox pair in eutectic LiCl–KCl–$CaCl_2$ with dilute $SnCl_2$ and dilute $SnCl_2$-$NiCl_2$ at 685 K is shown in Figures 23 and 24 respectively. The sharpness of the peaks is inconsistent with a soluble-soluble reaction. Rather, it is consistent with a surface constrained product (i.e., no outward diffusion of product), like the deposition peaks seen in the Sn^{2+}/Sn reaction CVs (see Figure 9). Furthermore, there is no indication of the volatilization of $SnCl_4$ at slow scan

rates as observed by Catrillejo. Cai et al. observed a similar CV to that of Castrillejo at 773 K with a graphite WE [11]. However, they found that the CV become less symmetrical at 773 K with a molybdenum WE.

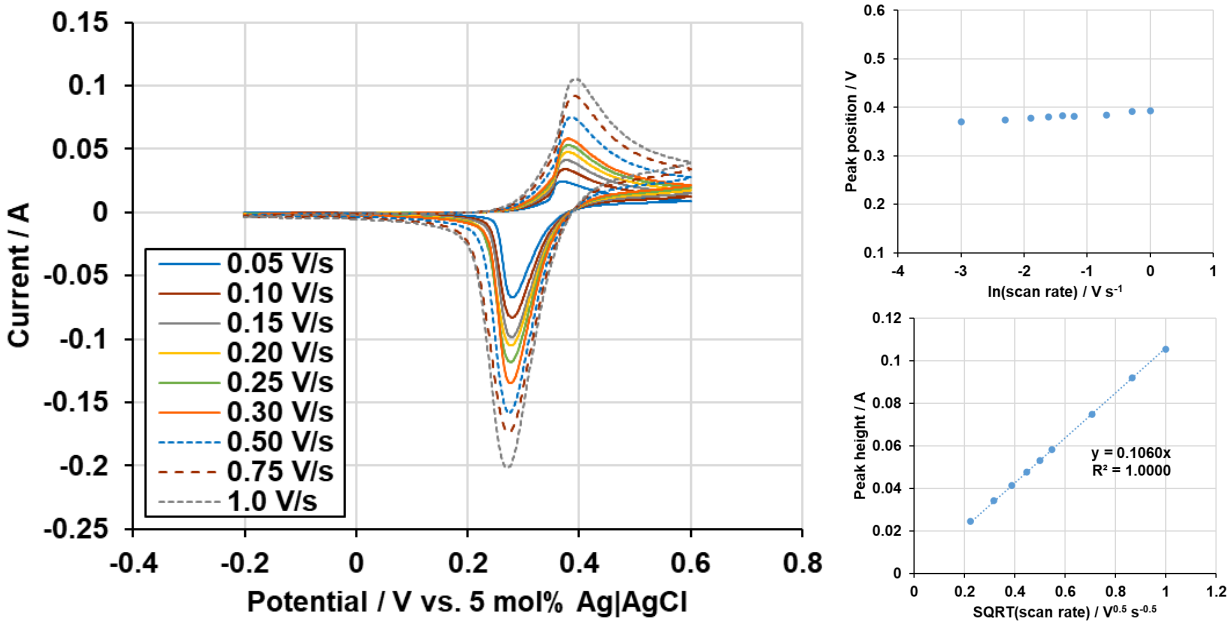

Figure 23: CV in LiCl-KCl-$CaCl_2$ eutectic salt for the soluble-insoluble Sn^{4+}/Sn^{2+} reaction at various scan rates from the $SnCl_2$ (6.5 x 10^{-5} mol cm^{-3}) system. WE: 1.5 mm W rod (0.812 cm^2), CE: 3.175 mm W rod, RE: 5 mol% Ag/AgCl, Temperature: 685 K, 88% IR compensation (0.22/0.25 Ω).

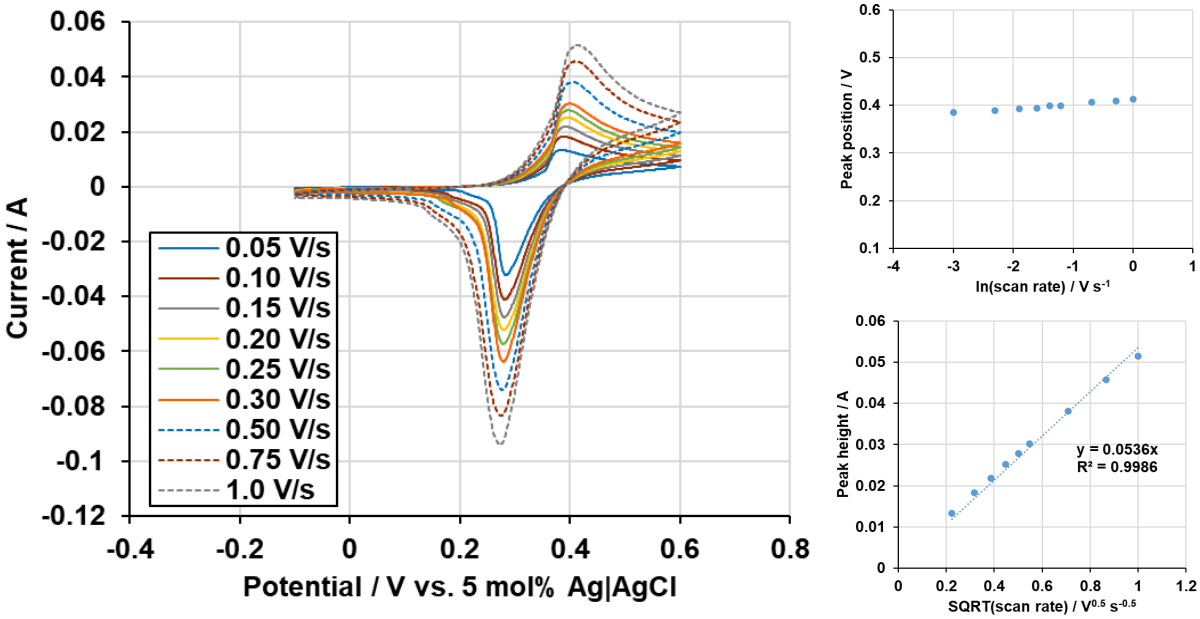

Figure 24: CV in LiCl-KCl-$CaCl_2$ eutectic salt for the soluble-insoluble Sn^{4+}/Sn^{2+} reaction at various scan rates from the $SnCl_2$(6.1 x 10^{-5} mol cm^{-3})-$NiCl_2$(6.8 x 10^{-5} mol cm^{-3}) system. WE: 1.5 mm W rod (0.506 cm^2), CE: 3.175 mm W rod, RE: 5 mol% Ag/AgCl, Temperature: 685 K, 94% IR compensation (0.37/0.395 Ω).

Ghallali et al. observed a similar CV to that shown in Figure 9 in LiCl−KCl eutectic salt at 673 K with a glassy carbon (GC) WE [3]. However, Ghallali found that the shape of the CV more closely resembled a soluble-soluble reaction as temperatures increased. At temperatures above 733 K, the CV became fully symmetrical, typical of a soluble-soluble reaction. Based on these observations, Ghallali concluded that at lower temperatures the oxidation of Sn^{2+} deposits an insoluble film on the WE. By increasing the temperature, the surface compound becomes soluble, and the shape of the peaks represents a classical soluble-soluble diffusion peak (i.e., inward diffusion of reactant, outward diffusion of product). A similar experiment was conducted in the LiCl−KCl−$CaCl_2$ eutectic with a tungsten WE, and the results can be seen in Figure 25. The results shown in Figure 25 differ from those of Ghallali et al. in that the insoluble film required a much higher temperature of 788 K before a fully soluble-soluble peak was observed.

As suggested by Ghallali et al., the temperature-dependent peak behavior likely reflects changes in product solubility. The observation of this behavior on both GC and tungsten electrodes indicates that it is independent of electrode material, ruling out $SnCl_4$–electrode interactions. A plausible candidate is solid K_2SnCl_6, which forms in the KCl-rich region of the KCl–$SnCl_4$ phase diagram and begins slowly decomposing at 623 K, with the maximum decomposition rate near 793 K, which is consistent with the observed transition to soluble–soluble behavior at 788 K [65, 66]. The lower transition temperature in LiCl–KCl (733 K) compared to LiCl–KCl–$CaCl_2$ suggests $CaCl_2$ may stabilize the insoluble product, possibly by slowing its thermal decomposition. Although the identity of the insoluble phase remains uncertain, K_2SnCl_6 is a feasible candidate based on phase behavior and decomposition characteristics.

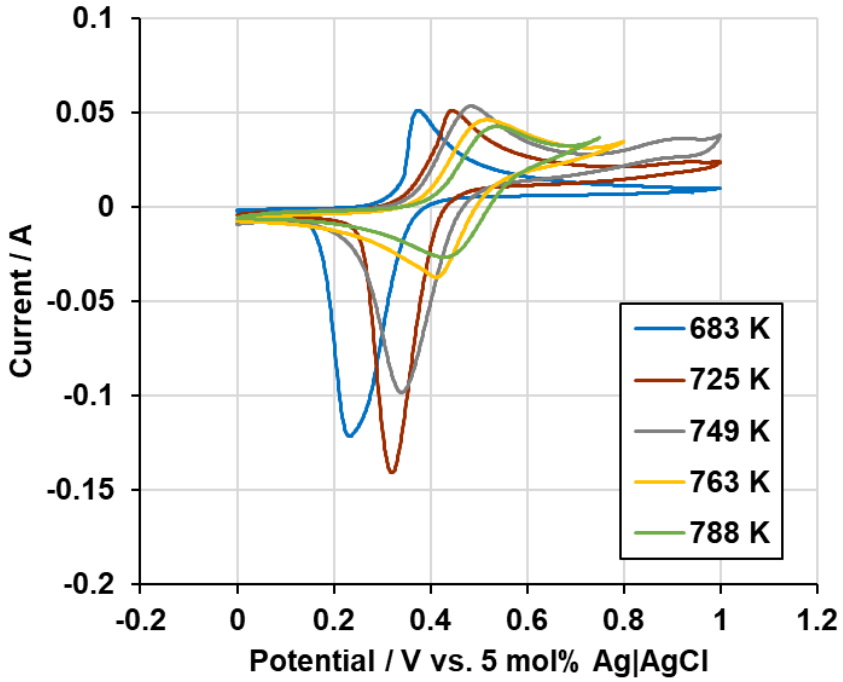

Figure 25: CV in LiCl-KCl-$CaCl_2$ eutectic salt for the Sn^{4+}/Sn^{2+} reaction at various temperatures from the $SnCl_2$ (1.8×10^{-5} mol cm^{-3}) system. WE: 1.5 mm W rod (0.672 cm^2), CE: 3.175 mm W rod, RE: 5 mol% Ag/AgCl, 82% IR compensation (0.14/0.17 Ω), scan rate: 0.1 V/s.

Multiple soluble-soluble CVs at different scan rates are shown for the Sn^{4+}/Sn^{2+} reaction at 788 K in Figure 26. At slower scan rates a smaller reduction peak at 788 K is observed, which is consistent with the loss of volatile $SnCl_4$. This is shown by the $I_{p,a}/I_{p,c}$ ratio trending down toward 1 as scan rate increases, as shown in the insert in Figure 26.

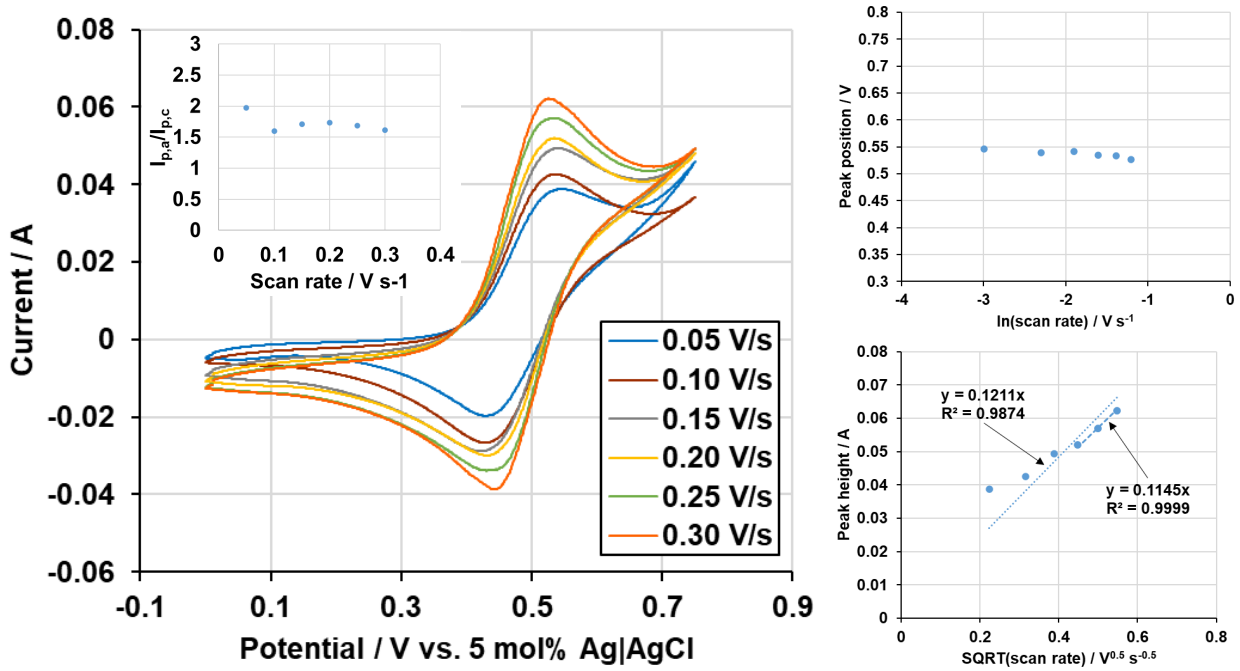

Figure 26: CV in LiCl-KCl-$CaCl_2$ eutectic salt for the soluble-soluble Sn^{4+}/Sn^{2+} reaction at various scan rates from the $SnCl_2$ (1.8 x 10^{-5} mol cm^{-3}) system. WE: 1.5 mm W rod (0.672 cm^2), CE: 3.175 mm W rod, RE: 5 mol% Ag/AgCl, Temperature: 788 K, 82% IR compensation (0.14/0.17 Ω).

Given the soluble-insoluble nature of the shape of the Sn^{4+}/Sn^{2+} peaks at 685 K, the CV measurements were analyzed using the Berzins-Delahay relationship (Eq. 3). At 788 K, where a soluble-soluble peak was observed, the Randles-Sevcik relationship was used. Additionally, the semi-integration method was used on both CV data sets. A summary of the calculated values in Table 7 shows that there is close agreement between the methods used to calculate the diffusivity for Sn^{2+} at 685 K. Furthermore, these values agree with those calculated using the same analytical methods on the Sn deposition peak (see Table 3).

Table 7: Calculated diffusivities for Sn^{2+} with and without Ni^{2+} present in LiCl-KCl-$CaCl_2$ from the Sn^{4+}/Sn^{2+} reaction CV data.

Species	Temperature (K)	Berzins-Delahay CV Diffusivity (10^{-5} cm^2 s^{-1})	Semi-integrated CV Diffusivity (10^{-5} cm^2 s^{-1})	Randles-Sevcik CV Diffusivity (10^{-5} cm^2 s^{-1})
Sn^{2+}	685	0.86 ± 0.06	0.99 ± 0.07	--
Sn^{2+} (w/ Ni^{2+})	685	0.64 ± 0.02	1.19 ± 0.05	--
Sn^{2+}	788	--	67.4 ± 6.5	41.3 ± 8.2

At 788 K, the departure from electrochemically reversible behavior at slower scan rates is shown in the lower-right insert of Figure 26. This is likely due to natural convection and/or a rise in background current indicated by the slight rise after the oxidation peak at ~0.65 V in Figures 25 and 26. At higher scan rates, natural convection becomes less influential and peak-to-background ratio increases minimizing the influence of background signals. The impact of

this behavior on the calculation of diffusivity is evident in the lower-right plot in Figure 26 by positive deviation from linearity at lower scan rates. The dotted-line represents the linear regression including all six CVs, and the dashed-line represents the linear regression including only the three CVs that appear to behave reversibly (0.20 V/s, 0.25 V/s, and 0.30 V/s). Only these three CVs were used to quantify the diffusivities of Sn^{2+} at 788 K as reported in Table 7.

3.8 Comparison of Diffusivities

Figure 27 summarizes the diffusivities calculated from each method and signal. Blue columns indicate individual values from each electroanalytical technique, with error bars showing confidence intervals. The strong overlap of these intervals and the proximity of individual values suggest that the true diffusivity is close to the average: $(1.03 \pm 0.10) \times 10^{-5}$ $cm^2 \cdot s^{-1}$ for Sn^{2+} and $(0.75 \pm 0.19) \times 10^{-5}$ $cm^2 \cdot s^{-1}$ for Ni^{2+}. The limited overlap between Sn^{2+} and Ni^{2+} intervals indicates that Ni^{2+} likely diffuses more slowly than Sn^{2+}. According to the Stokes–Einstein equation, a radius of the diffusion particle is inversely related to diffusivity. Ni^{2+} has a smaller ionic radius (78 pm) than Sn^{2+} (93 pm) and should diffuse faster, but this neglects complexation effects in molten salts. Complexation of Ni^{2+} and Sn^{2+} in LiCl–KCl or LiCl–KCl–$CaCl_2$ has not been well studied. However, $[SnCl_3]^-$ (pyramidal) and $[NiCl_4]^{2-}$ (tetrahedral) are known complexes of Sn^{2+} and Ni^{2+}, respectively. The additional Cl^- and tetrahedral geometry of $[NiCl_4]^{2-}$ likely make it larger than $[SnCl_3]^-$, consistent with the lower diffusivity of Ni^{2+}. Due to uncertainties in coordination, a definitive conclusion cannot be drawn, though the Ni^{2+} complex is likely larger than the Sn^{2+} complex.

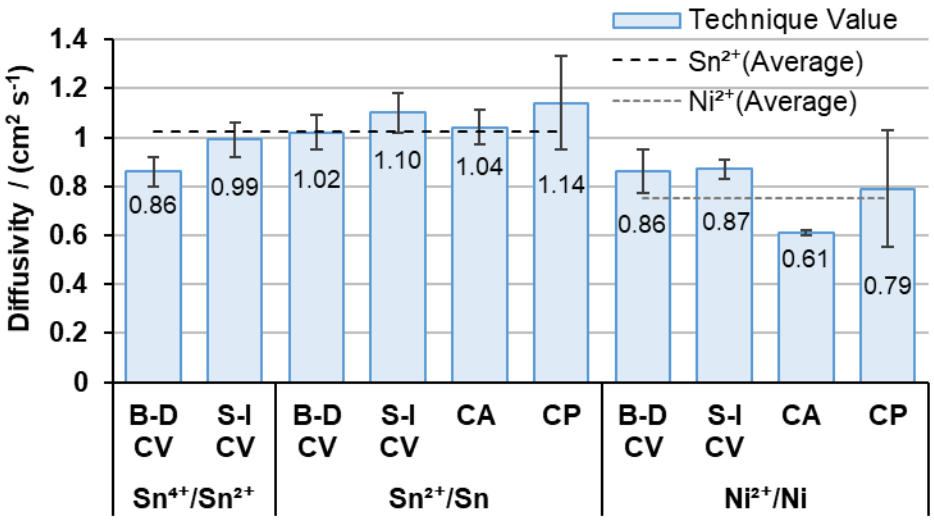

Figure 27: Summary of calculated diffusivities from each method for Sn^{2+} in LiCl-KCl-$CaCl_2$ at 685 K and for Ni^{2+} in LiCl-KCl-$CaCl_2$ at 683 K (B-D = Berzins-Delahay, S-I = Semi-Integral).

4.0 Conclusion

This comprehensive electrochemical analysis establishes key parameters for the Sn^{2+}/Sn redox couple in eutectic LiCl–KCl–$CaCl_2$ molten salt. The standard redox potential of Sn^{2+}/Sn was found to be –1.429 V vs. Cl_2/Cl^- when calculated using a molar concentration, consistent with prior studies in LiCl–KCl systems. Diffusivities for Sn^{2+} and Ni^{2+} were determined using multiple electrochemical techniques, with good agreement across methods. The presence of Ni^{2+} and Cu^+ impurities significantly influenced the electrochemical behavior of $SnCl_2$, reducing diffusivity and introducing alloy-related peaks. The diffusivity of Ni^{2+} is lower (0.75×10^{-5} $cm^2 \cdot s^{-1}$) than that of Sn^{2+} (1.03×10^{-5} $cm^2 \cdot s^{-1}$) indicating Ni^{2+} may form a larger complex than Sn^{2+}. Notably, the Sn^{4+}/Sn^{2+} redox couple exhibited a transition from surface-constrained to soluble-soluble behavior at elevated temperatures, with volatility of $SnCl_4$ limiting its analytical utility above 788 K.

Due to proximity of Cu^+/Cu and Sn^{2+}/Sn signals and standard reduction potentials, electrochemical separation of Cu and Sn is limited, and other separation schemes are recommended. However, sufficient separation of Ni^{2+}/Ni and Sn^{2+}/Sn standard reduction potentials supports the suitability of electrochemical separation of Ni from Sn. Knowing the standard reduction potentials of Ni and Sn is critical to separation selectivity and optimization. These results offer valuable insights into the feasibility of selective electrochemical separation of Sn in complex molten salt systems and lay the groundwork for future modeling and process optimization in nuclear and metallurgical applications.

5.0 Acknowledgements

This work was primarily supported by Battelle Savannah River Alliance, LLC under Contract No. 89303321CEM000080 with the U.S. Department of Energy. The United States Government retains a non-exclusive, paid-up, irrevocable, world-wide license to publish or reproduce the published form of this manuscript, or allow others to do so, for United States Government purpose. Some of the time spent by Bryant Johnson, Ricardo Ceron, and Devin Rappleye in preparing this manuscript was funded by Lawrence Livermore National Laboratory (LLNL) under the auspices of the U.S. Department of Energy (DOE) under Contract No. DE-AC52-07NA27344. The authors thank the Brigham Young University Department of Chemistry Spectroscopic Facility for access to the ICP-MS instrument.

6.0 References

1. Xu L, Ge T, Chen G, et al (2023) Recycling of waste indium tin oxide target for In-Sn alloy production based on molten salt electrochemistry. J Environ Chem Eng 11:109858. https://doi.org/10.1016/j.jece.2023.109858

2. Qin B, Cui P, Martinez AM, Haarberg GM (2019) Electrochemical Behavior of Tin in Molten LiCl-KCl at 450 °C. Int J Electrochem Sci 14:1407–1415. https://doi.org/10.20964/2019.02.53

3. El Ghallali H, Groult H, Barhoun A, et al (2009) Electrochemical synthesis of Ni–Sn alloys in molten LiCl–KCl. Electrochimica Acta 54:3152–3160. https://doi.org/10.1016/j.electacta.2008.11.051

4. Groult H, El Ghallali H, Barhoun A, et al (2010) Preparation of Co–Sn alloys by electroreduction of Co(II) and Sn(II) in molten LiCl–KCl. Electrochimica Acta 55:1926–1932. https://doi.org/10.1016/j.electacta.2009.11.010

5. Große M, Lehmann E, Steinbrück M, et al (2009) Influence of oxide layer morphology on hydrogen concentration in tin and niobium containing zirconium alloys after high temperature steam oxidation. J Nucl Mater 385:339–345. https://doi.org/10.1016/j.jnucmat.2008.12.021

6. Liao J-J, Yang Z-B, Qiu S-Y, et al (2019) Corrosion of New Zirconium Claddings in 500 °C/10.3 MPa Steam: Effects of Alloying and Metallography. Acta Metall Sin Engl Lett 32:981–994. https://doi.org/10.1007/s40195-018-0857-7

7. Chipman G, Johnson B, Choi S, et al (2023) Determination of a surrogate for plutonium electrorefining. J Radioanal Nucl Chem 586:154680. https://doi.org/10.1016/j.jnucmat.2023.154680

8. Zhang C, Parkes AM, Holliday KS (2023) First principles optimization of plutonium electrorefining. J Nucl Mater 577:154327. https://doi.org/10.1016/j.jnucmat.2023.154327

9. Laitinen HA, Liu CH (1958) An Electromotive Force Series in Molten Lithium Chloride-Potassium Chloride Eutectic. J Am Chem Soc 80:1015–1020. https://doi.org/10.1021/ja01538a001

10. Shafir JM, Plambeck JA (1973) Thallium and Tin Electrode Potentials in Fused LiCl–KCl Eutectic. Can J Chem 51:1693–1696. https://doi.org/10.1139/v73-254

11. Cai Y, Chen X, Xu Q, Xu Y (2018) Electrochemical Behaviour of Tin in a LiCl-KCl Eutectic Melt. Int J Electrochem Sci 13:10786–10797. https://doi.org/10.20964/2018.11.21

12. Pasquier P, Ferry D, Picard G (1990) Etude thermodynamique et cinetique du systeme electrochimique Sn(II)/Sn dans l'eutectique LiCl□KCl A 723 K. Electrochimica Acta 35:905–911. https://doi.org/10.1016/0013-4686(90)90088-H

13. Pasquier P, Picard GS (1992) Pit-mapping procedure for obtaining charge transfer kinetic parameters from steady state current-potential curves. Electrochimica Acta 37:1149–1152. https://doi.org/10.1016/0013-4686(92)85237-F

14. Delarue G (1960) Propriétés chimiques dans l'eutectique LiCl-KCl fondu I. Oxydes métalliques. J Electroanal Chem 1959 1:285–300. https://doi.org/10.1016/0022-0728(60)85029-2

15. Combes R, Vedel J, Trémillon B (1970) Standard potential determinations in molten NaCl-KCl. J Electroanal Chem Interfacial Electrochem 27:174–177. https://doi.org/10.1016/S0022-0728(70)80217-0

16. Gaur HC, Behl WK (1963) Polarographic studies in molten magnesium chloride-sodium chloride-potassium chloride eutectic. J Electroanal Chem 1959 5:261–269. https://doi.org/10.1016/0022-0728(63)80039-X

17. Francini M, Martini S (1968) Oscillographic polarography in molten nitrates—III. The behaviour of oxygen and its ions. Electrochimica Acta 13:851–861. https://doi.org/10.1016/0013-4686(68)85018-2

18. Munday TCF, Corbett JD (1966) An Electromotive Force Study of Lower Oxidation States of Lead, Cadmium, and Tin in Molten $NaAlCl_4$. Inorg Chem 5:1263–1268. https://doi.org/10.1021/ic50041a042

19. Sherer CS (1972) The role of alkali metal cations in Lux-Flood acid-base reactions in fused salt media. J Inorg Nucl Chem 34:1615–1619. https://doi.org/10.1016/0022-1902(72)80283-5

20. Xu X, Hussey CL (1993) The Electrochemistry of Tin in the Aluminum Chloride-1-methyl-3-ethylimidazolium Chloride Molten Salt. J Electrochem Soc 140:618–626. https://doi.org/10.1149/1.2056132

21. Castrillejo Y, García MA, Martinez A-M, et al (1997) A comparative study of the electrochemistry of tin ions in the ZnCl2 + xNaCl mixtures at 450°C. J Electroanal Chem 434:43–53. https://doi.org/10.1016/S0022-0728(97)00101-0

22. Yasuda K, Nohira T, Ogata YH, Ito Y (2005) Electrochemical window of molten LiCl–KCl–CaCl2 and the Ag+/Ag reference electrode. Electrochimica Acta 51:561–565. https://doi.org/10.1016/j.electacta.2005.05.014

23. Sri Maha Vishnu D, Sanil N, Mohandas KS, Nagarajan K (2016) Electrochemical characterisation of CaCl 2 deficient LiCl–KCl–CaCl 2 eutectic melt and electro-deoxidation of solid UO 2. J Nucl Mater 470:179–186. https://doi.org/10.1016/j.jnucmat.2015.12.003

24. Guo L, Zuo P, Zhang Z, et al (2023) A Review of Cu–Ni–Sn Alloys: Processing, Microstructure, Properties, and Developing Trends. Materials 16:444. https://doi.org/10.3390/ma16010444

25. Raabe D (2023) The Materials Science behind Sustainable Metals and Alloys. Chem Rev 123:2436–2608. https://doi.org/10.1021/acs.chemrev.2c00799

26. Williams T, Torrie J, Schvaneveldt M, et al (2024) Electrochemical Identification of Metal Chlorides in Eutectic LiCl-KCl Without Prior Knowledge of Analyte Identities. Nucl Technol 1–17. https://doi.org/10.1080/00295450.2024.2348849

27. Chipman G, Johnson B, Vann C, et al (2024) Experimental determination of the electrochemical properties of bismuth chloride in eutectic LiCl–KCl and LiCl–KCl–CaCl2 molten salts. J Radioanal Nucl Chem 333:1119–1135. https://doi.org/10.1007/s10967-024-09354-4

28. Fuller R, Williams T, Schvaneveldt M, Rappleye D (2022) A comparison of square-wave voltammetry models to determine the number of electrons exchanged in metal deposition. Electrochimica Acta 414:140220. https://doi.org/10.1016/j.electacta.2022.140220

29. Fatouros N, Krulic D (2013) Analysis of the square wave voltammetry for reversible metal deposition on a foreign substrate – Experimental study of silver deposition on gold. J Electroanal Chem 706:76–85. https://doi.org/10.1016/j.jelechem.2013.07.019

30. Rappleye DS, Fuller RG (2023) Bringing the Analysis of Electrodeposition Signals in Voltammetry Out of the Shadows. J Electrochem Soc 170:063505. https://doi.org/10.1149/1945-7111/acd879

31. Aoki K, Tokuda K, Matsuda H (1986) Reversible square-wave voltammograms independence of electrode geometry. J Electroanal Chem 207:25–39

32. Barker GC, Faircloth RL, Gardner AW (1956) SQUARE WAVE POLAROGRAPHY, PART IV, AN INTRODUCTION TO THE THEORETICAL ASPECTS OF SQUARE WAVE POLAROGRAPHY. Great Britain Atomic Energy Research Establishment, Harwell, Berks, England (United Kingdom)

33. Berzins T, Delahay P (1953) Oscillographic polarographic waves for the reversible deposition of metals on solid electrodes. J Am Chem Soc 75:555–559

34. Grenness Morten, Oldham KB (1972) Semiintegral electroanalysis. Theory and verification. Anal Chem 44:1121–1129

35. Williams T, Shum R, Rappleye D (2021) Review—Concentration Measurements In Molten Chloride Salts Using Electrochemical Methods. J Electrochem Soc 168:123510. https://doi.org/10.1149/1945-7111/ac436a

36. Randles JEB (1948) A cathode ray polarograph. Part II.—The current-voltage curves. Trans Faraday Soc 44:327–338. https://doi.org/10.1039/TF9484400327

37. Ševčík A (1948) Oscillographic polarography with periodical triangular voltage. Collect Czechoslov Chem Commun 13:349–377. https://doi.org/10.1135/cccc19480349

38. Cottrell FG (1903) Der Reststrom bei galvanischer Polarization, betrachtet als ein Diffusionsproblem. Z Phys Chem Stöchiom Verwandschaftsl 385–431

39. Sand HJS (1901) III. *On the concentration at the electrodes in a solution, with special reference to the liberation of hydrogen by electrolysis of a mixture of copper sulphate and*

sulphuric acid. Lond Edinb Dublin Philos Mag J Sci 1:45–79. https://doi.org/10.1080/14786440109462590

40. Bard AJ, Faulkner LR, White HS (2022) Electrochemical Methods - Fundamentals and Applications, 3rd ed. John Wiley & Sons, Ltd

41. Russell CD, Peterson JM (1963) Interpretation of totally irreversible chronopotentiometric waves. J Electroanal Chem 1959 5:467–475. https://doi.org/10.1016/0022-0728(63)80055-8

42. Fitzhugh RL, Clark AD, Nickerson SD, et al (2021) On the Electrochemical Thermodynamics of Minor Components in Molten Salt Mixtures. J Electrochem Soc 168:026502. https://doi.org/10.1149/1945-7111/abdd7c

43. Navidi W (2014) Statistics for Engineers & Scientists, 4th ed. McGraw Hill

44. Skoog DA, Holler FJ, Crouch SR (2017) Principals of Instrumental Analysis. In: Principals of Instrumental Analysis, 7th ed. pp 10–15

45. Plambeck JA (1967) Electromotive force series in molten salts. J Chem Eng Data 12:77–82. https://doi.org/10.1021/je60032a023

46. Barin I (1995) Thermochemical Data of Pure Substances, 1st ed. Wiley

47. Zhang W, Pulham CR, Mount AR, et al (2008) Thermodynamic calculation and reference electrode calibration for high temperature molten salts. Energy Mater 3:132–136. https://doi.org/10.1179/174892408X394254

48. Shen M, Li B, Yu J (2012) Investigation on electrochemical removal of CaCl2 from LiCl–KCl melts. Electrochimica Acta 62:153–157. https://doi.org/10.1016/j.electacta.2011.12.007

49. Xu Q, Schwandt C, Fray DJ (2004) Electrochemical investigation of lithium and tin reduction at a graphite cathode in molten chlorides. J Electroanal Chem 562:15–21. https://doi.org/10.1016/j.jelechem.2003.07.032

50. Wang J, Han J, Jung I-H, et al (2014) Thermodynamic optimizations on the binary Li–Sn system and ternary Mg–Sn–Li system. Calphad 47:100–113. https://doi.org/10.1016/j.calphad.2014.07.001

51. Palenzona A, Manfrinetti P, Fornasini ML (2000) Phase diagram of the Ca–Sn system. J Alloys Compd 312:165–171. https://doi.org/10.1016/S0925-8388(00)01150-6

52. Liu Z, Lu G, Yu J (2021) Investigation on electrochemical behaviors of Ni(II) impurity in LiCl-KCl melt. Sep Purif Technol 268:118354. https://doi.org/10.1016/j.seppur.2021.118354

53. Liu HS, Wang J, Jin ZP (2004) Thermodynamic optimization of the Ni–Sn binary system. Calphad 28:363–370. https://doi.org/10.1016/j.calphad.2004.12.002

54. Islam F, Medraj M (2005) The phase equilibria in the Mg–Ni–Ca system. Calphad 29:289–302. https://doi.org/10.1016/j.calphad.2005.08.006

55. Schmetterer C, Flandorfer H, Richter KW, et al (2007) A new investigation of the system Ni-Sn. Intermetallics 15:869–884

56. Mendelsohn MH, Gruen DM, Krauss AR (1986) Recent results on the preparation and properties of Li-Containing Cu alloys. J Nucl Mater 141–143:184–187. https://doi.org/10.1016/S0022-3115(86)80033-2

57. Bruzzone G (1971) The binary systems calcium-copper, strontium-copper and barium-copper. J Common Met 25:361–366. https://doi.org/10.1016/0022-5088(71)90178-0

58. Shim JH, Oh CS, Lee BJ, Lee DN (1996) Thermodynamic assessment of the Cu-Sn system. Z Fuer Met 87:205–212

59. Wang Y, Li M, Zhang M, et al (2018) Electrochemical deposition of praseodymium (III) and copper (II) and extraction of praseodymium on copper electrode in LiCl-KCl melts. J Solid State Electrochem 22:3689–3702. https://doi.org/10.1007/s10008-018-4080-2

60. Cai Y, Liu H, Xu Q, et al (2015) Investigation on the reaction progress of zirconium and cuprous chloride in the LiCl–KCl melt. Electrochimica Acta 161:177–185. https://doi.org/10.1016/j.electacta.2015.02.078

61. Cai Y, Chen X, Xu Y, Xu Q (2022) *In situ* electrochemical investigation of the reaction progress between Zr and a CuCl–$SnCl_2$ mixture in a LiCl–KCl molten salt. RSC Adv 12:4135–4144. https://doi.org/10.1039/D1RA08889K

62. Gou S-P, Sun I-W (2008) Electrodeposition behavior of nickel and nickel–zinc alloys from the zinc chloride-1-ethyl-3-methylimidazolium chloride low temperature molten salt. Electrochimica Acta 53:2538–2544. https://doi.org/10.1016/j.electacta.2007.10.039

63. Porat Z (2024) Electrochemical Characterization of Diffusion in Polymeric vs. Monomeric Solvents. Int J Mol Sci 25:4472. https://doi.org/10.3390/ijms25084472

64. Yoon D, Baggett A, Phongikaroon S, et al (2019) Fundamental Data Acquisition toward Silver-Silver Chloride Reference Electrode. J Electrochem Soc 166:E159–E164. https://doi.org/10.1149/2.0721906jes

65. Zalewicz M (1987) Examination of the thermal decomposition of chlorostannates(IV). Thermochim Acta 116:217–224. https://doi.org/10.1016/0040-6031(87)88181-9

66. The American Ceramic Society and the National Institute of Standards and Technology (2025). Phase Equilibria Diagrams Online Database (NIST Standard Reference Database 31). Figure 7268